Spring 5-2014

An Investigation of Quantum Dynamics in a Three-Level Bose-Einstein Condensate System

Saad J. Ansari
Bates College, sansari@bates.edu

Recommended Citation

Ansari, Saad J., "An Investigation of Quantum Dynamics in a Three-Level Bose-Einstein Condensate System" (2014). *Honors Theses*. 89.
http://scarab.bates.edu/honorstheses/89

An Investigation of Quantum Dynamics in a Three Level Bose-Einstein Condensate System

Saad J. Ansari

Department of Physics and Astronomy, Bates College, Lewiston, ME

An Investigation of Quantum Dynamics in a Three-Level Bose-Einstein Condensate System

An Honors Thesis

Presented to the Department of Physics and Astronomy

Bates College

in partial fulfillment of the requirements for the

Degree of Bachelor of Science

by

Saad J. Ansari

Lewiston, Maine

March 21,2014

To Father, Mother, Hamza and Talha

Abstract

Bose-Einstein condensates present to us the opportunity to probe into the atomic interactions that govern a macroscopic quantum mechanical system. The degenerate hyperfine manifold in the bosonic atoms splits in the presence of an external B-field; radio-frequency induced coupling releases experimentally-attainable knowledge about the Zeeman manifold in ^{87}Rb. The purpose of this study is to investigate quantum dynamics in two and three-component Bose-Einstein condensate (BEC) systems. We start with a theoretical analysis of Josephson tunneling dynamics between identical BECs trapped in a double potential well, paying particular attention to the non-linear self-trapping effect observed as a consequence of the intra-well interaction. We present a model for the non-equilibrium dynamics in a two-level system and introduce the Rabi oscillations. This is followed by a numerical and experimental investigation of Rabi oscillations in a three-level ^{87}Rb BEC between the $F = 1$ hyperfine level spin states $m_F \in \{-1, 0, 1\}$. The relation between the observed *total Rabi frequency*, Ω_R and the detuning Δ, along with its effect on the BEC population dynamics is explored. Finally, we explore the possible suspects for the shift of the resonance at strong Rabi frequencies Ω.

Contents

List of Figures

Acknowledgments

It has been quite a journey, with many sleepless nights may I add. If there is anyone responsible for me being here, it has to be my advisor, Nathan. Working with him this past year has truly redefined my boundaries of knowledge. He has been a constant source of inspiration throughout this amazing time, believing in the kids when we needed it the most, he is truly the ‘legend’ . The amazing physics crew, in Joanna, Eddie and Chris, this document may well have remained an unscripted dream if it wasn’t for you guys. We started together and we pushed that button together, you guys are winners. Eddie, you and your quirky comments, planned to perfection, sometimes even too cool to be true, really made life so much fun in these tough times. Chris, you really don’t know how naturally gifted you are, never lose that positive attitude. You invigorated and helped bring the best out oof me so often.was more than invigorating throughout this process. And of course, Joanna, your clever choice of words, at just the right times, did wonders for me, beyond your imagination. And Josh, i couldn’t have asked for a better roommate over these four amazing years, except maybe for your failure to beat me at FIFA. And you albert, with all the funny moments in the carnegie basement, they couldn’t have come at a better time. You guys did more for me than you can imagine.

I cannot start a new chapter in my life without acknowledging all that the Physics department has done for me. It was unlike anything I had ever been a part of. From day one, I was welcomed with open arms. I was a naive teenager from the third world...and you transformed me. I must thank Michael Durst and Hong Lin, who have always been there when need I needed a shoulder. And of course, Mark Semon. You are single-handedly the best individual I have met at Bates. Your desire to take challenges head on and keep fighting until the problem itself gives up, has taught me to never 'err', to never lose hope, and to always believe that anything is possible.

My brothers Hamza and Talha, we have seen some truly amazing times. You have more been a blessing for our family. With you two achieving all the milestones that you did, it always inspired me to do my utmost best in the hardest of times. You are the elder brothers every guy wishes for.

And most importantly of all, mom and dad. You have sacrificed so much to enable us get to where we are. Without you, the world truly seems a daunting place. Your belief in me was inspiring; it got me going when I was down and out. I can't thank you enough for all the prayers and everything that you have done.

Chapter 1

Introduction to Bose-Einstein Condensation

Whilst lecturing the students in 1924 at the University of Dhaka, Sathyandra Nath Bose's intent was to show the inadequecy of the theory of radiation in comparison to the experimental data. A simple statistical error in his approach instead led to a theory satisfying the experiment. In his 'Planck's Law and the hypothesis of light quanta' [**5**], Bose probed into the statistics of identical indistinguishable particles. While Bose's ideas were initially dismissed by the physics community, Albert Einstein saw the importance of his results and extended it to predict the existence of a novel low-temperature state of matter, the 'Bose-Einstein condensate'. Einstein showed that at extremely low temperatures, the probability that a particle occupies the ground energy level is very high [**6**]. At this stage the inter-particle separation is very small compared to the particles' De Broglie wavelength [**7**], and the wave-like atoms start to overlap. In this 'super-atom', the quantum features of the individual atoms are greatly amplified, a behavior better known as macroscopic quantum phenomena [**8**] .

In this section, we will start by introducing the topic of quantum statistics and various particle distributions to the reader (Section 1.1). Next, a brief section on the theory of

Bose-Einstein condensation (Section 1.2) will be followed by a discussion of the properties of the ^{87}Rb atom, including the fine, hyperfine and the zeeman manifold of the alkali atom (Section 1.3). The final section will look at the ingenious and yet inexpensive laser cooling techniques after some 80 years of development (Section 1.4). A roadmap for this thesis will be presented in Section 1.5.

1.1. Quantum Statistics

As illustrated by quantum mechanics and its experimental success, the world is governed by probabilities. No matter how bizarre this idea may seem to a fatalist [**9**], this is exactly how the quantum world appears to us again and again[1] (at least for now). One of the hallmarks of Thermal Statistics, the Gibbs distribution gives a measure of the probability of a system to occupy a state s with energy ϵ_s and number of particles N. More explicitly stated, the Gibbs factor (1.1) gives the occupancy probability for defined values of s, ϵ_s, N and the chemical potential μ [**10**].

$$e^{\left(\frac{(N\mu - \epsilon_s)}{k_B T}\right)} \tag{1.1}$$

The sum of the Gibbs factors forms the normalization factor for state probabilities. The Gibbs sum Z, or the grand partition function, is completed over all states s and the number of particles N in a system (1.2). Here, $\lambda = e^{(\mu/k_B T)}$ for the case of an ideal gas

---

[1] The probabilistic nature of the world rarely features in the contested aspects of quantum mechanics. On the other hand, the sudden collapse of the wave function has been the main focus of multiple physics and even philosophical debates.

(non-interacting dilute gas), as in [**11**].

$$Z(\mu, T) = \sum_{N=0}^{\infty} \sum_{s} e^{\left(\dfrac{(N\mu - \epsilon_s)}{k_B T}\right)} = \sum_{N=0}^{\infty} \sum_{s} \lambda^N e^{\left(\dfrac{-\epsilon_s}{k_B T}\right)} \tag{1.2}$$

Then, the probability that the system will be in a state of energy ϵ with particles N is given by (1.3)

$$P(\epsilon, N) = \frac{\lambda^N e^{(-\epsilon_s/k_B T)}}{Z} \tag{1.3}$$

In quantum mechanics, indistinguisable particles come in two types. Fermions are particles with a half integral spin (1/2,3/2,5/2,...etc), and their distribution across states is governed by the Pauli exclusion principle [**12**]. On the other hand, bosons are particles with an integral spin (1,2,3,...etc) and therefore not subject to Pauli exclusion; bosons have no restrictions on the occupancy number per particle state. For the fermions (e.g. quarks, electrons) no identical two fermions can occupy the same quantum state in a system. Only in the quantum regime, does the identity of such particles start to dictate their distribution.

In the classical regime, it is virtually impossible to identify the bosonic or fermionic nature of particles simply based off the particle distribution across the energy states[2]. The average occupancy per state is much less than 1 for both bosons and fermions for this classical case. As we head into the quantum regime, the bosonic distribution is squeezed down; the bosons abandon the energetic quantum states and settle into the ground state of the system. For a fermionic distribution in the same environment, the Pauli Exclusion

---

[2] The distribution functions for both bosons and fermions converge to the same limit at everyday (not ultra-cold) temperatures.

principle ensures that only a single fermion occupies the ground state and as a result, the average occupancy per state is close to, but always less than, 1.

For our derivations of these new distributions, we will consider only two states. A particle can either occupy the state invoking our curiousity (then it will be part of the system), or it will be part of the reservoir (which does in fact contain numerous states, but for our purposes, all that matters is the exchange between the system and reservoir). The thermal average of the occupancy of the system in a state s with energy ϵ is represented by $n(\epsilon_s)$ (1.4). Meanwhile, the total number of atoms is given simply by the sum of all the average state occupancies $n(\epsilon_s)$ (1.5).

$$n(\epsilon_s) = \frac{\sum_{N=0}^{\infty} \sum_s N\lambda^N e^{(-\epsilon_s/k_B T)}}{Z} \tag{1.4}$$

$$N = \sum_s n(\epsilon_s) \tag{1.5}$$

For a distribution of fermions, the average occupancy per state cannot exceed 1 (a consequence of the Pauli Exclusion principle). In this case, the partition function Z only contains two terms (1.6), and the average occupancy $n(\epsilon)$ can be simplified into an expression similar to (1.7). This is the **Fermi-Dirac distribution**, which gives the average fermion occupancy per state at a temperature T.

$$Z_{FD} \rightarrow 1 + \lambda e^{-\frac{\epsilon}{k_B T}} \tag{1.6}$$

$$n_{FD}(\epsilon) = \frac{1}{e^{(\epsilon-\mu)/(k_B T)} + 1} \tag{1.7}$$

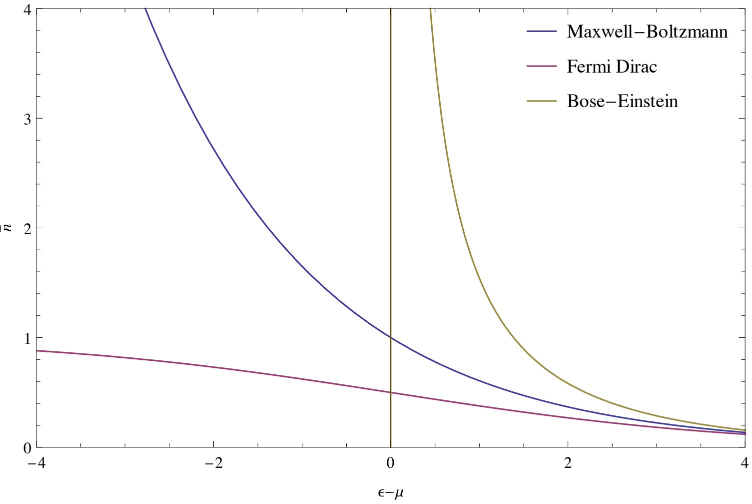

FIGURE 1.1. In the classical limit (at large values of $\epsilon - \mu$), all the distributions converge to the same function.

The partition function for a distribution of bosons can be summed up by looking at individual terms of the series and noting that it converges to a limit (1.8) [**11**]. We find that the the average occupancy of a state is given by (1.9). This is the famous **Bose-Einstein distribution function**.

$$Z_{BE} \rightarrow \frac{1}{1 + \lambda e^{-\frac{\epsilon}{k_B T}}} \tag{1.8}$$

$$n_{BE}(\epsilon) = \frac{1}{e^{(\epsilon-\mu)/(k_B T)} - 1} \tag{1.9}$$

We see that both the Fermi-Dirac and the Bose-Einstein distributions approach the same limit in the classical regime. At normal temperatures, the energy of a system is large, i.e. $\epsilon - \mu$ is a large number. All the distribution functions converge to the same average occupancy function $n(\epsilon)$ (Figure 1.1). This is the reason why it can be hard to distinguish between bosonic and fermionic systems simply based off information about $n(\epsilon)$ at a room-like temperature T.

1.2. Theory of the Bose-Einstein Condensate

The defining property of bosons is the ability for multiple bosons to occupy the same quantum state or orbital. We see from (1.9) that as $T \to T_c$, where T_c is the critical temperature specific to the atoms under consideration, the average occupancy for the ground state of the distribution ($n_{BE}(\epsilon = 0)$) becomes macroscopically large. At this low energy scale, the Heisenberg Uncertainty principle dictates the emergence of a large uncertainty in a particle's position, and atoms start to behave like waves. The macroscopic overlap of the de Broglie waves of identical bosons leads to the creation of a wave-like super-atom in the ground state (Figure 1.2). This happens when the inter-atom separation reduces to a number smaller than the thermal de Broglie wavelength of the atoms; More precisely, this phase transition occurs when $n{\lambda_{DB}}^3 > 2.612$, where n is the particle density and $\lambda_{DB} = h/\sqrt{2\pi m k_B T}$ is the thermal de Broglie wavelength of a particle [**13**]. Typically, condensation to a solid or liquid happens long before atoms reach this regime. The BEC is a supercooled metastable state, which can only be achieved at low atomic densities. At high densities, the rate of three body collisions is high, converting the atoms into molecules, and works against the condensate. Therefore, it is vital to keep the condensate at a low particle density, in order to increase its lifetime. Such densities can only be achieved in an ultrahigh vacuum chamber. A condensate lifetime can range from a few seconds to a minute in a typical vacuum chamber.

After some 70 years of development and research on laser-cooling techniques (briefly reviewed in Section 1.4), Bose-Einstein condensation was first observed in 1995 at JILA, where Eric Cornell and Carl Weiman were able to Bose condense ^{87}Rb atoms, achieving

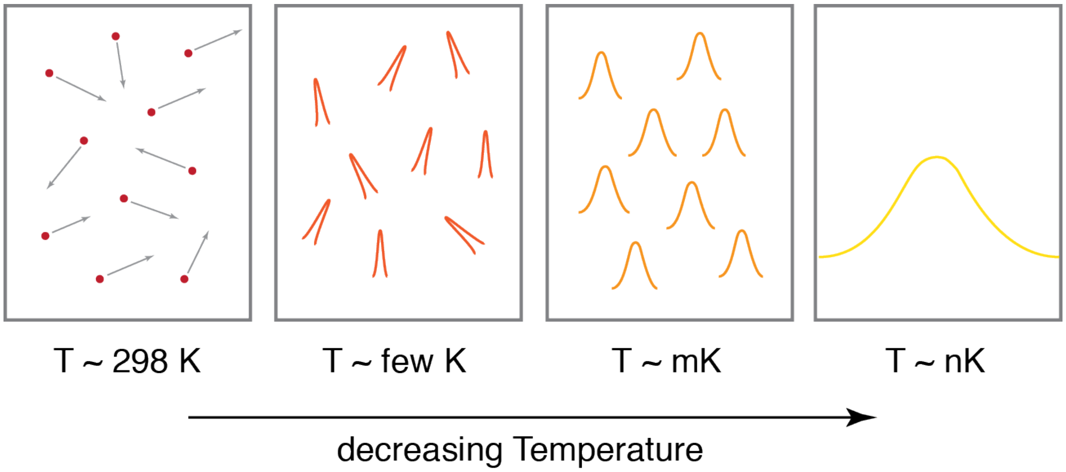

FIGURE 1.2. As the temperature decreases and we head into the quantum regime, atoms shift from being point-like particles to wave-like distributions. The overlap of waves is so dramatic that the atoms lose their individual identity, and become a part of a super atom. Adapted from [**1**].

a condensate density of $2.5 * 10^{12}$ cm^{-3} atoms at a temperature of 170 nK [**14**]. Four months later, Wolfgang Ketterle at MIT was able to produce a ^{23}Na condensate with about a hundred times more atoms [**1**]. The high number of atoms enabled Ketterle to observe quantum mechanical interference effects between two condensates. This milestone meant that the three pioneers of ultracold atomic physics shared the Nobel Prize in 2001.

1.3. Atomic Structure of Rubidium

Alkali-metals have a near-monopoly in BEC labs around the world. The first ever condensate was created with the 87-isotope of Rubidium [**14**]. Rubidium has two bosonic isotopes: ^{85}Rb and ^{87}Rb. ^{85}Rb nucleus is the stable isotope, while the ^{87}Rb nucleus decays to ^{87}Sr with a half-life of $4.97(3)10^{10}$ years [**15**]. There are a multitude of reasons for the popularity of ^{87}Rb: The ^{87}Rb isotope has 37 protons, 37 electrons and 50 neutrons; In total, the atom has 124 fermions, which makes the ^{87}Rb isotope a boson. Its convenient splitting of 780.24 nm between the $5^2S_{1/2}$ and the $5^2P_{3/2}$ states (Figure 1.3) means that we can use a relatively inexpensive diode laser, lasing in the near-infrared range, to bump the atoms into the first excited state, $5^2P_{3/2}$.

The orbital and spin angular momentum for the ^{87}Rb atom is determined by the nuclear spin and the valence electrons. The presence of a single valence electron greatly simplifies the theory. This section is meant to be a selective review of a collegiate quantum physics course for the interested reader. In what follows, we will review the fine, hyperfine and zeeman theory as applied to the ^{87}Rb atom.

The *fine structure* is a result of the spin-orbit coupling in the electron's inertial frame and the relativistic energy correction. In the electron's frame, the nucleus orbits around the electron, producing a magnetic field $\mathbf{B}$ that interacts with the electron's magnetic moment. We define the quantum number J by the relation in (1.10), where L is the orbital angular momentum and $S = 1/2$ is the spin angular momentum. The $n = 5$ level contains the 5s and the 5p orbital (corresponding to $L \in \{0, 1\}$). The fine structure is composed of 5^2X_J levels. For an electron occupying the 5s orbital, $J \in \{1/2\}$ for $L = 0$ ($X \to S$). For an electron occupying the 5p orbital, $J \in \{1/2, 3/2\}$ where $L = 1$ ($X \to P$). As this degeneracy is lifted, the $n = 5$ level transitions into the *fine* energy levels $5^2S_{1/2}$ or $5^2P_{1/2}$ and $5^2P_{3/2}$ (depending on the electron's occupation of the s or the p-orbital).

$$|L - S| \leq J \leq L + S \tag{1.10}$$

The nucleus of an atom has a magnetic moment which creates a B-field. The interaction of the electron's angular momentum with the magnetic field of the nucleus leads to the *hyperfine manifold*. The total angular momentum F is given by (1.11) where I is the nuclear spin.

$$F = J + I \tag{1.11}$$

$$|J - I| \leq F \leq J + I \tag{1.12}$$

For this regime, F is the "good" quantum number (or the conserved quantity). The ^{87}Rb isotope has a total of 37 protons, of which there is only unpaired proton, which occupies the $2p_{3/2}$ nuclear orbital [**16**]. Hence, the isotope has a total nuclear spin $I = 3/2$ [**2**]. Then, Table 1 follows from (1.11) and (1.12).

J	I	F
$1/2\ (L \to 0)$	$3/2$	$1, 2$
$1/2\ (L \to 1)$	$3/2$	$1, 2$
$3/2\ (L \to 1)$	$3/2$	$0', 1', 2', 3'$

TABLE 1. The hyperfine manifold for $L = 0$ and $L = 1$ states; it is shown (not to scale) in Figure 1.3

The hyperfine splitting is given by 1.13 where A_{hfs} is the magnetic dipole constant and B_{hfs} is the electric quadrupole constant (not applicable for states with $J = 1/2$). For the ground state ($5^2S_{1/2}$) of ^{87}Rb, A_{hfs} has been experimentally determined through atomic-fountain measurements to be 3.417 GHz [**17**]. For the ground state, $K \to (-1/2 \pm 2)$. This corresponds to an energy gap of 6.835 GHz between the $F = 1$ and the $F = 2$ hyperfine manifold.

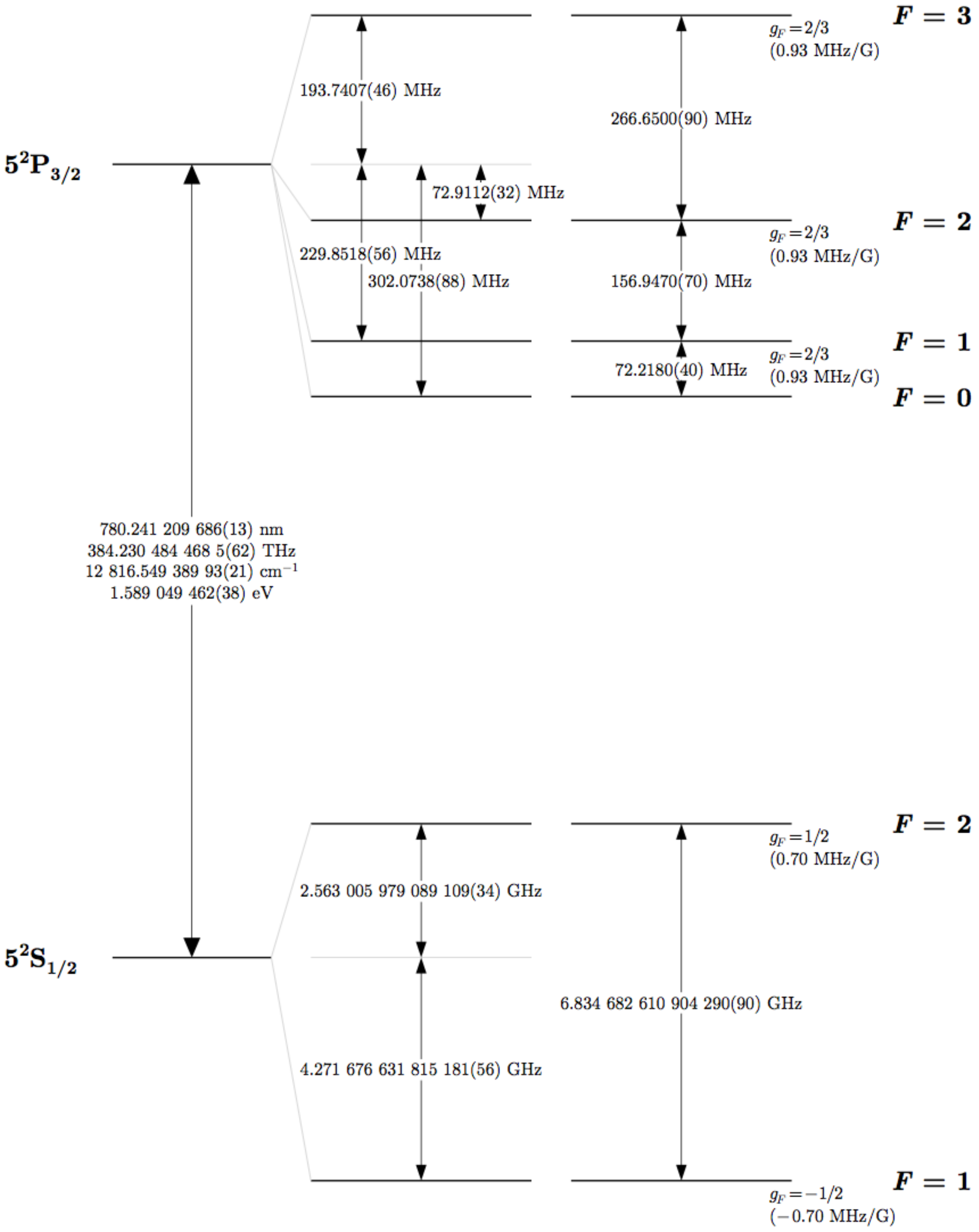

FIGURE 1.3. The D_2 Rubidium Fine and Hyperfine structure. We encourage the reader to consult the original source of this figure [**2**]. The Lande-g factors for the hyperfine structure are included along with the Zeeman shift per unit of Gauss. Note that these numbers only represent the Zeeman shifts in the weak magnetic field linear regime.

$$\Delta E_{hfs} = \frac{1}{2}A_{hfs}K + B_{hfs}\left(\frac{\frac{3}{2}2K(K+1) - 2I(I+1)J(J+1)}{2I(2I-1)2J(2J-1)}\right) \tag{1.13}$$

$$K = F(F+1) - I(I+1) - J(J+1) \tag{1.14}$$

$$\Delta E_{5^2S_{1/2},hfs} = \frac{1}{2}A_{hfs}\left(F(F+1) - I(I+1) - J(J+1)\right) \rightarrow 6.835GHz \tag{1.15}$$

The presence of an external magnetic field produces another perturbation, the *Zeeman shift*. The energy splitting is introduced by the alignment of the atomic magnetic moment along the direction of the external magnetic field. As a result, each hyperfine degenerate manifold gets split up into $2F+1$ Zeeman sub-levels (represented by $|F, m_F|$). m_F is the new quantum number which represents the projection of the magnetic moment along B_z.

In the Zeeman splitting regime, $F = 1$ level has a degeneracy of 3, which gets lifted in the presence of an external magnetic field. The excitation frequencies for each Zeeman sublevel are slightly different. In a weak field scenario, the difference is given by (1.16), where μ_B is the Bohr Magneton, g_F is the Lande g-factor, and B_z is the z-component of the magnetic field. Knowing g_F for the ground states ($g_F = \pm 1/2$) and excited states ($g_F = 2/3$) enables us to determine the change in excitation frequency $\Delta\omega = \Delta E/\hbar$.

$$\Delta E = \mu_B g_F m_F B_z \tag{1.16}$$

In a strong external magnetic field, the Zeeman splittings are no longer linear. The Paschen-Back effect comes into play, which is a result of the external field disrupting the coupling between the orbital (L) and spin (S) angular momenta. Then, the energy

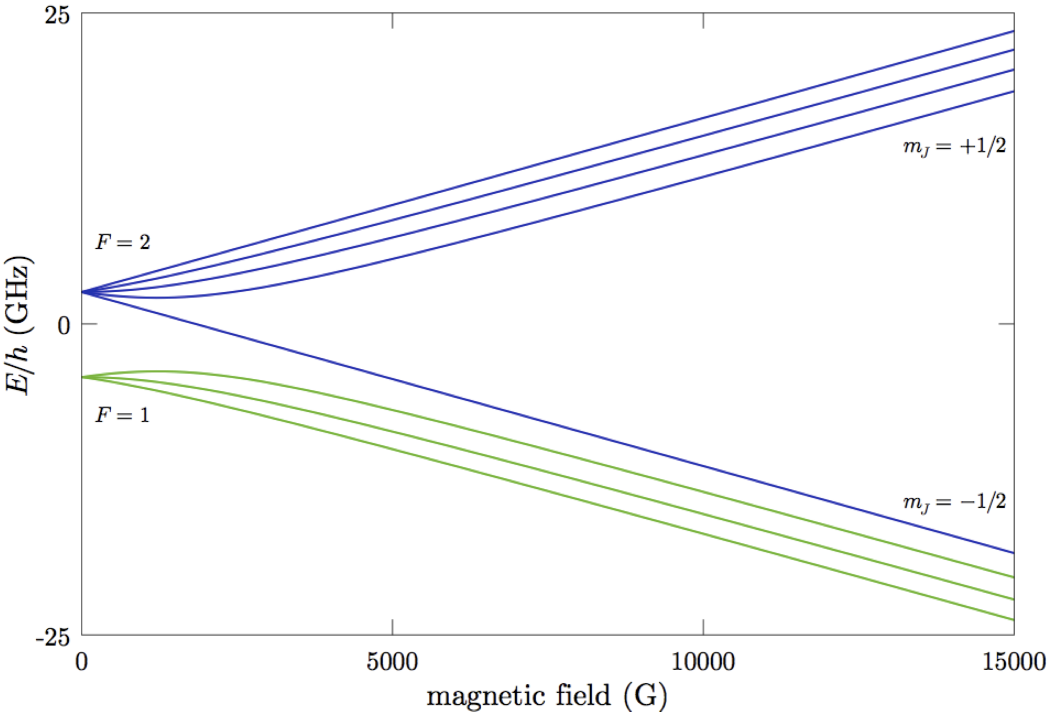

FIGURE 1.4. The splitting for the hyperfine manifold of the ground state $5^2S_{1/2}$ of ^{87}Rb in presence of an external magnetic field (in units of Gauss). In the weak Zeeman field, the splitting is represented by the F values. In the strong Zeeman field scenario, the splitting is represented by the values for m_J.

splitting is given by the Breit-Rabi formula (1.17). A plot of the Breit-Rabi equation is presented in Figure 1.4.

$$E_{BR,(F=3/2\pm1/2)} = \frac{\Delta E_{hfs}}{2(2I_1)} - \mu_B g_I m_F B \pm \frac{\Delta E_{hfs}}{2}\sqrt{1 + \frac{4}{2I+1} m_F x B + (xB)^2} \qquad (1.17)$$

where

$$x = \frac{\mu_B(g_J - g_I)}{\Delta E_{hfs}}$$

The frequency shift is different for different Zeeman sub-levels; this plays an important role during laser-cooling, with certain atoms becoming more likely to absorb a certain frequency than the other. In the next section, we will review the cooling techniques (developed over the course of 70-80 years) that have gone into the experimental realization of the Bose-Einstein condensate

1.4. The Atomic Refrigerator: Laser Cooling

Experimentalists have spent the better half of a century developing cooling techniques to realize the Bose-Einstein condensate. This section will be a review of the theory of laser cooling, including the Zeeman slower, Optical Molasses and the Magneto-Optical Trap (MOT). Finally we will review the technique of “evaporative cooling”, which enables cooling below the Doppler limit. For a more detailed description of the entire cooling process, we refer the curious reader to [**18, 19**].

Speaking in the broadest terms possible, the atoms are heated in an oven and then bombarded with a monochromatic laser in the Zeeman Slower. These events take place in an ultrahigh vacuum chamber, ensuring that our condensate agent is not affected by stray atoms in the apparatus. Every absorbed photon also brings about a momentum kick in the direction opposite to atom propagation. This is the force of light and it drastically reduces the atom temperatures. Next, the atomic beam is subjected to counter-propagating beams (one in each of the 3 dimensions). In this ’optical molasses’ phase, atoms are further cooled down to the Doppler temperature. A position-dependent magnetic force strives to hold the atoms from the optical molasses at the center of trap. This forms the *magneto* part of the MOT.

After cooling in the MOT, atoms are held in a harmonic magnetic trap, ready for evaporative cooling. Radio-frequency radiation resonant at a radius from the trap center enables hot atoms (with strong oscillations) to transition out of the trap, and hence leave the remaining atoms a little colder than before. This process of evaporative cooling, applied for a range of radio-frequencies, single-handedly cools the trapped atoms. As the thermal cloud ejects its hottest atoms, the temperature decreases into the nK regime and the phase-space density increases to the point where macroscopic quantum effects become observable. The Bose-Einstein condensate is formed, which behaves like a super-atom and can be experimented on and then released from the trap for imaging. Shadow imaging is used to determine its position and density, while time-of-flight measurements probe into its momentum-data. Imaging techniques will be briefly reviewed at the end of this section.

1.4.1. Zeeman Slower

The first stage of the cooling process requires an almost-steady flow of gaseous atoms. A chunk of metal (^{87}Rb in our Bates Lab) is heated in an effusive oven, maintained in an ultrahigh vacuum chamber, and the gaseous atoms (at about $370K$) exit through a gate into the Zeeman Slower. In our Bates ultracold laboratory, we utilize a tapered single-layer solenoid with a zero crossing. For a thorough understanding of the construction of the Zeeman Slower, we refer the reader to the thesis “Progress Towards Bose-Einstein Condensation” by previous student Marc Tollin ’12.

As the atoms propagate through the solenoid, they are met with the Zeeman Slower beam, which propagates opposite to the atomic beam. The laser appears blue-shifted by an amount that depends on the reference frames of different atoms. Let us track a group of atoms which enter the Zeeman Slower at, say 350 ms^{-1} and are hit with a detuned laser beam. A magnetic field inside the solenoid then shifts the resonant frequency of the high-speed atoms bringing them into resonance with the laser beam. The angular detuning Δ from resonance in an atom's reference frame is dependent on both the Zeeman shift (due to $B_{solenoid}$) and the Doppler shift (due to $v \neq 0$) (1.18). By substituting (1.16) here for a specific energy level, we can find the strength of the magnetic field B in the axial direction of the solenoid. As the fast atoms absorb the now-resonant photons, they receive a momentum-kick slowing them down. As the atoms slow down, the effective detuning Δ (1.18) also changes. The magnetic field inside the solenoid is varied to make up for the change in detuning. In this way we can, in a sense, lock on to the fastest atoms and shrink the Maxwell-Boltzmann distribution. An alternate, but less popular method is to sweep our Zeeman laser frequency to always stay in resonance with the decelerating atoms instead of varying the magnetic field, a method known as "chirp" cooling.

$$\Delta = \Delta_0 + \frac{2\pi v}{\lambda} + \frac{\Delta E}{\hbar} \tag{1.18}$$

The fast atoms absorb the now-resonant photons, which carry both energy and momentum (1.19). When absorbed, a photon excites an atom into an excited state, and also provides a momentum-kick in the opposite direction. Some time later, the atom will spontaneously emit a photon in a random direction. When considering large numbers, the spontaneous photon emission gets averaged out to zero, and in general, the overall momentum change is in the direction of the laser beam.

$$p = \frac{\hbar\omega}{c} \tag{1.19}$$

In the Zeeman slower, atoms are decelerated from about 330 ms^{-1} to 30 ms^{-1} in about 0.7 meters.

1.4.2. The Magneto-Optical Trap

In the next phase, we load the ^{87}Rb vapor into a Magneto-Optical Trap (MOT) (Figure 1.4.2), which, as the name suggests, makes use of optical kicks and magnetic forces to slow down and trap the alkali atoms. Six counter-propagating laser beams (two in each of the 3 dimensions) form an "optical molasses". The lasers are slightly red-tuned away from resonance of cold atoms, which brings it into resonance with the hotter atoms. The optical molasses simply slows down the faster atoms (some very fast/hot atoms may still be able to escape). The quadrupole magnetic trap, which employs the anti-Helmholtz configuration creates a potential minimum at the center of the MOT. As a result, cold atoms remain stranded in the middle while hotter atoms undergo ultra-damped oscillations about the potential minimum.

The lasers exert a scattering force on the hotter atoms on resonance and slow them down, so they can be trapped by the quadrupole trap. In this MOT, atoms are cooled all the way down to their Doppler limit ($T \rightarrow 14z0\mu K$). The fact that even such low temperatures are insufficient for Bose-Einstein condensation shows the daunting task that

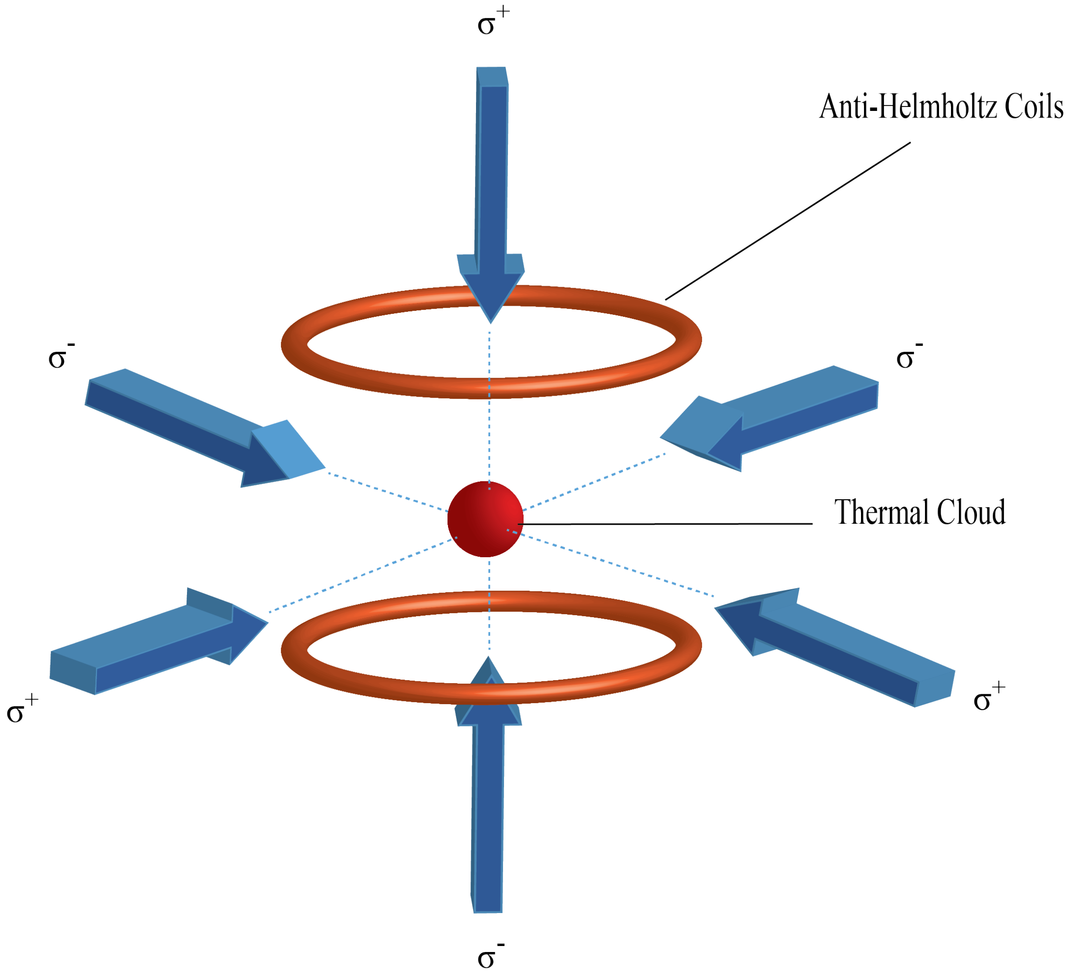

FIGURE 1.5. The Magneto-Optical Trap. The figure shows six counter-propagating beams in the **x**, **y** and **z** directions along with two magnetic coils in an anti-helmholtz configuration (the current in both coils is anti-parallel). Adapted from [**3**].

we once faced as experimentalists. For sub-doppler cooling into the nK-regime, still hotter atoms need to be traded out of the thermal cloud in exchange for a temperature drop.

1.4.3. Evaporative Cooling

This is the final stage of the BEC creation process; it is necessary to reduce the temperature below the critical temperature T_c. Once the MOT is turned off, the atoms from the optical molasses are loaded into a harmonic magnetic trap. The hotter the atoms are, the higher they can climb up the potential. The trap depth is reduced significantly until the potential depth is about 100 nK, so that the most energetic atoms now have enough energy to escape the trap. During a rethermalization phase, the atoms also undergo collisions and some more hotter atoms escape the trap. This "evaporative cooling" technique allows us to get the temperature below the critical value, and achieve Bose-Einstein condensation.

In our Radio-Frequency (RF)-induced magnetic trap, we are resonant with atoms away from the center of the trap (at a radius r from the trap) to excite the hotter atoms into an untrappable state and out of the thermal cloud. The magnetic field gradient means that we can express the trap height as a function of the RF. A sweep of the RF laser allows us to remove the hotter atoms from the cloud. At this point in time, the thermal cloud is cold enough, that the atoms overlap each other and form a condensate, with a single macroscopic wavefunction (Figure 1.2).

1.4.4. Imaging

Once the condensate is formed, information about its atomic distribution can be obtained by releasing it, and allowing it to undergo ballistic expansion. Probing the condensate with a resonant laser beam, this "time of flight" technique, allows us to obtain absorption images of the BEC. A typical condensate image is shown in Figure 1.6. It is color-coded to represent the atomic density, increasing from blue to green to yellow to red. The presence of a magnetic field gradient means that different Zeeman sublevels will feel forces in different directions.

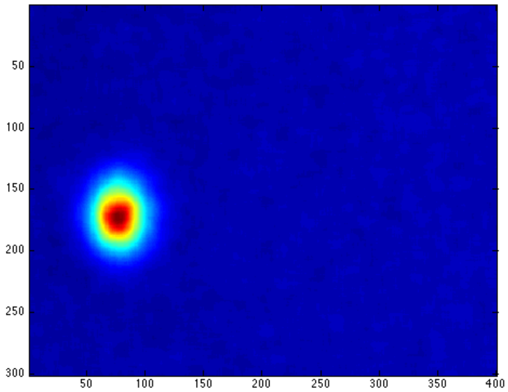

FIGURE 1.6. Absorption Image of a ^{87}Rb condensate in the $|F=1, m_F=1\rangle$ Zeeman state.

The force on a condensate particle is given by (1.20). In our lab, we utilize the ground states of ^{87}Rb. The $|F=1, m_F=1\rangle$ and $|F=1, m_F=-1\rangle$ Zeeman sublevels have opposite magnetic momenta μ, while the $|F=1, m_F=0\rangle$ sublevel does not have an associated magnetic moment. From (1.20), it follows that the two former sublevels ($m_F=\pm1$) will feel a force in opposite directions, while the middle sublevel ($m_F=0$) will feel no force.

$$\vec{F} = -\nabla U = \nabla(\vec{\mu}.\vec{B}) \rightarrow \mu \nabla B \tag{1.20}$$

For a spinor condensate, a condensate with multiple spin-components (atoms in all three $F=1$ Zeeman states), a typical image is presented in Figure 1.7. This is the famous Stern-Zerlach technique used to obtain information about atomic angular momenta [**20**]. Our experimental data (Chapter 4) have been extracted using this technique.

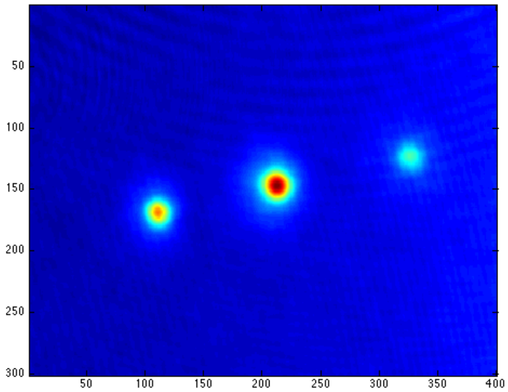

FIGURE 1.7. Absorption Image of a ^{87}Rb condensate occupying the $|F = 1, m_F = 0, \pm 1\rangle$ Zeeman state. The condensate is separated using the Stern-Gerlach technique in the presence of a magnetic field gradient.

1.5. A Roadmap

> *Our field is now at a historic turning point, in which we are moving from studying physics in order to learn about atom cooling to studying cold atoms in order to learn about physics.* J.R. Anglin and W. Ketterle [**21**]

Investigating the amplified quantum dynamics in cold atoms has brought us a giant step closer to understanding atom-atom interactions at the scale of a single atom, and how they affect the "big picture". Cold atoms are perfect testing grounds to expand our knowledge of coupled multi-level systems, both in the hyperfine and the Zeeman manifold. This thesis is organized as follows:

- Our first inquiry will focus on an interactive Bose gas. An introduction of the Gross-Pitaeskii equation is followed by a detour into a theoretical review of the superconductive Josephson junction. We then investigate the novel population and phase dynamics of a condensate in a symmetric double-well trap, and discuss the similarities to its superconductive counter-part (Chapter 2)

- In the world of Spinor condensates, we discuss the theory of a two-level BEC system, in the "interaction picture", when coupled due to an electromagnetic driving field. The Rabi oscillations and the effects of detuning from resonance on the state probabilities are discussed (Chapter 3).
- In Chapter 4, we extend the two-level theory to a three-level system in the interaction picture, and predict Rabi oscillations associated with the *Rabi frequency* Ω. The ground state of ^{87}Rb splits into 3 different Zeeman levels $|1,1\rangle$,$|1,0\rangle$ and $|1,-1\rangle$ under the influence of an external magnetic field. We study this radio-frequency coupled three-level system in our ultracold atomic lab, and perform numerical analysis to fit the observed features to our Rabi theory. We observe the effects of non-zero detuning on the state probabilites in Fourier space, and report an observed shift of the resonance ω_0 at strong driving field Ω. The thesis concludes by investigating the coherence time of our condensate.

Throughout the thesis, footnotes and citations are used to guide the curious reader towards useful resources. We encourage the utilization of these for certain derivations and lengthy calculations, in order to make this document more comprehensible for the reader. In Figures $4.2--4.7$, the labels for P_0 and P_2 should be replaced to be consistent with the experimental conditions. In Figures $4.2--4.7$, a labeling statement like $\Omega \rightarrow 2\pi(300)$ KHz should be replaced by $\frac{\Omega}{2\pi} \rightarrow 300$ KHz. A further correction to the units should be included in Figures 4.3 and 4.7; here a labeling statement like $\omega_0 \rightarrow 3.8x10^6$ rad s^{-1} should be changed to $\frac{\omega_0}{2\pi} \rightarrow 3.8$ MHz.

Chapter 2

Josephson Dynamics in an Interactive Bose Gas

The atomic dynamics in a condensate are responsible for its novel nature. Since the condensate is really just an overlap of thousands, or even millions of wavefunctions, we can model it using quantum mechanics. In this chapter, we will discuss the internal dynamics of a single condensate, when held in a harmonic trap. We will draw an exciting relation to superconductivity, and discuss the behavior of a superconductor in the Josephson Junction. Finally, we will talk about two condensates trapped in a double-well. The remarkable unified behavior, including the self-trapping phenomena will be introduced in the last section.

2.1. Gross-Pitaevski Equation: An Interactive Picture

The quantum-mechanical BEC is modeled as an N-particle system. We assign the wavefunction $\Psi(\vec{r})$ to the system, and individual wavefunctions $\psi(\vec{r_i})$ to the individual atoms at spatial positions $\vec{r_i}$. Then, the multi-particle wavefunction $\Psi(\vec{r})$, can be expressed using the Hartee-Fock approximation as the product of all the individual $\psi(\vec{r_i})$ as follows.

$$\Psi(\vec{r}) = \psi(\vec{r_1}) \otimes \psi(\vec{r_2}) \otimes ... \otimes \psi(\vec{r_i}) \tag{2.1}$$

In order to model our system we need to include its potential, kinetic and internal dynamics. The first two are taken care of by the Schrödinger equation for a particle (2.2), and we can modify it to to include the effects due to interaction. We make an addition of a non-linear interaction term, $g|\psi|^2$ on the right hand side. This is the Gross-Pitaeskii equation (2.3), first presented by Eugene P. Gross and Lev P. Pitaeskii in 1961 to describe the ground state of a quantum system of identical bosons.

$$i\hbar\frac{\partial\psi}{\partial t} = \left(-\frac{\hbar^2}{2m}\nabla^2 + V_{external}\right)\psi, \tag{2.2}$$

$$i\hbar\frac{\partial\psi}{\partial t} = \left(-\frac{\hbar^2}{2m}\nabla^2 + V_{external} + g|\psi|^2\right)\psi \tag{2.3}$$

The applications of this equation are such that it can be used to study superfluid and superconductive systems [**8**]. For our Bose gas, we assume that each particle has an individual wavefunction and feels an external wavefunction, which remains the same for all particles in the system. This is the mean-field approximation which simply states that each particle feels the presence of the same environment as every other particle in the system. This method works very well in dilute quantum systems where the interactions are generally weak. This enables us to rewrite (2.1) as (2.4) and normalize the system wavefunction $\langle\Psi \mid \Psi\rangle = 1$.

$$\Psi(\vec{r}) = \psi(\vec{r}) \otimes \psi(\vec{r}) \otimes ... \otimes \psi(\vec{r}) \tag{2.4}$$

The effective Hamiltonian can be written as (2.5) where $U_0 = 4\pi\hbar^2 a/m$ is the constant effective interaction at low energies [**22**], and a is the s-wave scattering length.

$$\mathbf{H} = \sum_{i=1}^{N} \left[-\frac{\hbar^2}{2m}\frac{\partial^2}{\partial \vec{r_i}^2} + V(r_i) \right] + U_0 \sum_{i<j} \delta(\vec{r_i} - \vec{r_j}) \tag{2.5}$$

Let us now attempt to minimize the free energy $F = E - \mu N$ where $E(\psi) = \frac{\langle \psi \,|\, \hat{H} \,|\, \psi \rangle}{\langle \psi \,|\, \psi \rangle}$. This gets reduced to minimizing $F(\psi) = \langle \psi \,|\, H \,|\, \psi \rangle - \mu \langle \psi \,|\, \psi \rangle$. Calculating this, our expression for F becomes (2.6) based off [**23**].

$$\begin{aligned} F = &-N\frac{\hbar^2}{2m}\int \psi^*(\vec{r})\nabla^2\psi(\vec{r})d\vec{r} + N\int \psi^*(\vec{r})V_{ext}\psi(\vec{r})d\vec{r} \\ &+ \frac{N(N-1)}{2}U_0 \int d\vec{r} \int \psi^*(\vec{r})\psi(\vec{r'})\delta(\vec{r}-\vec{r'})\psi(\vec{r})\psi(\vec{r'})d\vec{r'} \\ &+ \mu\left(\int \psi^*(\vec{r})\psi(\vec{r})d\vec{r}\right)^N \end{aligned} \tag{2.6}$$

We employ the variational technique [**23**] to minimize F and set $\frac{\partial F}{\partial \psi^*} = 0$. Solving for each of the terms before recombining them, we obtain for the variation:

$$\begin{aligned} \frac{\delta F}{\delta \psi^*} = 0 = N\int \Bigg[&-\frac{\hbar^2}{2m}\nabla^2\psi(\vec{r}) + V_{ext}(\vec{r})\psi(\vec{r}) \\ &+(N-1)U_0\left(\int |\psi(\vec{r})|^2\delta(|\vec{r}-\vec{r'}|)d\vec{r'}\right)\psi(\vec{r}) - \mu\psi(\vec{r})\Bigg]\delta\psi^*(\vec{r})d\vec{r} \end{aligned}$$

We minimize the free energy F by setting the expression inside the square brackets equal to zero. Substituting in for U_0 and approximating $N-1 \simeq N$, we obtain the time-independent Gross-Pitaevskii equation (2.7). The scattering length a can be either positive or negative, which leads to either an attractive or repulsive condensate; the s-wave scattering length sets the tone for the condensate's future. It is positive for ^{87}Rb ($109a_0$) and negative for ^{7}Li ($-23.3a_0$) [**24**]. Note that (2.7) is the same as the time-independent Schrödinger equation except for the addition of an external potential, a non-linear $U_0|\psi(\vec{r})|^2$. On the right hand side, the eigenvalue for the Hamiltonian is the chemical potential (which may or may not be equal to the energy E per particle, depending on uniformity of the condensate).

$$-\frac{\hbar^2}{2m}\nabla^2\psi(\vec{r}) + V_{ext}(\vec{r})\psi(\vec{r}) + N\frac{4\pi\hbar^2}{m}a|\psi(\vec{r})|^2\psi(\vec{r}) = \mu\psi(\vec{r}) \tag{2.7}$$

In the case of a uniform Bose gas, the GPE reduces to:

$$\mu = U_0|\psi(\vec{r})|^2 = U_0 n \tag{2.8}$$

The GPE predicts remarkable features in multi-condensate systems. The resulting mathematics is similar to that of a coupled system with a barrier; we will come back to discuss the GPE for BEC trapped in a double harmonic potential well in the last section of this chapter.

2.2. The Superconductive Josephson Junction

The Bose Einstein condensate is not the only system where the overlap of atomic ψ leads to an amplification of quantum phenomena. Exciting effects have been observed in certain kinds of fluids (superfluidity) and metals (superconductivity) at low temperatures. Superconductivity is the phenomena of zero electrical resistivity displayed by certain materials at temperatures close to absolute zero (for Type-I superconductors) [**25**]. When a material transitions to its superconductive phase, it also expels environmental magnetic flux, exhibiting the Meissner effect [**26**]. For a complete understanding of the BCS theory of superconductivity, we refer the reader to [**25, 26, 27**].

In superconductive physics, a pair of electrons can make a bound state as a result of phonon interactions in a lattice. These 'Cooper' pairs are duo-fermion systems, which means that they are bosons (integral spin). As the temperature drops below the critical temperature, the 'Cooper' pairs drop to their ground state as a result of Bose-Einstein condensation. We can employ quantum mechanics to ascribe a wavefunction ψ and a relative phase ϕ to a superconductor. We define ψ in terms of the Cooper pair density ρ and the relative phase of the pairs ϕ(2.9).

$$\psi = \sqrt{\rho}\exp\left[i\phi\right] \tag{2.9}$$

When two superconductors are placed close together, separated only by an insulating barrier, there are "super shorts" observed. In 1962, Brian Josephson (at the age of 22) attempted to solve the problem, and associated the short-circuit not to a breach in the barrier but to the tunneling of Cooper pairs [**28**] through the barrier. This amplification of quantum phenomena, as hypothesized by Josephson, was met with fierce opposition from Bardeen and Cooper [**29**].

Consider two superconductors, sandwiched together with a barrier. Then, we can model their behavior with a modified Schrödinger equation (2.10). The coeffecient α is an interaction parameter due to the insulating barrier and represents the strength of the coupling between the two superconductive systems.

$$i\hbar\frac{\partial}{\partial t}\psi_{A,B} = H_{A,B}\psi_{A,B} + \alpha\psi_{B,A} \tag{2.10}$$

We can also define the wavefunctions $\psi_{A,B}$ as in (2.11), where ϕ is the relative phase between the two electrons in the Cooper pairs.

$$\psi_{A,B} = \sqrt{\rho_{A,B}}\exp\left[i\phi_{A,B}\right] \tag{2.11}$$

We can algebraically solve (2.10) by employing (2.11) and equating the real and imaginary parts. We obtain the relations (2.12) [**30**]. The positive sign goes with superconductor A, and the negative sign is used when considering superconductor B.

$$\frac{\partial}{\partial t}\rho^*_{A,B} = \pm\frac{2}{\hbar}\alpha\sqrt{(\rho_A\rho_B)^*}\sin\varphi \tag{2.12}$$

Upon inspection of relation (2.12), we can make deductions about the behavior of the coupled superconductors. Even though there is a tendency for the the pair density ρ to change, in reality this would lead to a charge imbalance and create an electric field. The absence of an electric field in the barrier suggests that the magnitude of the rate of change of pair densities must be the same for both superconductors. The current density J through the barrier depends on the charge and the rate of change of ρ (2.13)

$$J = e^*\frac{\partial\rho}{\partial t} = \frac{4e}{\hbar}\alpha\sqrt{(\rho_A\rho_B)}\sin\varphi \tag{2.13}$$

The maximum current density can be defined as J_c, which leads to the first Josephson equation (2.14)

$$J = e^* \frac{\partial \rho}{\partial t} = J_c \sin \varphi \tag{2.14}$$

The phase difference φ between the superconductors changes with time, and so there is an oscillating current density with a maximum value of J_c. This is a result of Cooper pair tunneling through the insulating barrier. We observe similar quantum features in a Bose gas trapped in multiple potential wells.

2.3. Josephson Dynamics in a Bose gas

The ability to assign a single wavefunction to macroscopic systems means that different systems of particles in significantly different environments could end up acquiring a similar 'one-body' wavefunction. The coherent behavior of bosons in a Bose-Einstein Condensate allows us to ascribe to the condensate a single wavefunction. This ψ should be sufficient, along with an equation of dynamics (The Gross-Pitaevskii equation) to describe all of its exhibited properties, including the quantum tunneling phenomena.

In this section, we will look at a non-ideal weakly-linked BEC in a symmetric double-well trap (Figure 2.3) for $E_1^0 - E_2^0 \rightarrow 0$. We will present theoretically predicted dynamics of atomic tunneling for a BEC at zero temperature.

For a condensate trapped in this asymmetric double-well (we will enforce the limit of a symmetric trap later in the derivation), we define the zero point energies of the two wells as E_1^0 and E_2^0, and the number of particles in each of the wells are N_1 and N_2, such that $N = N_1 + N_2$, where N is the total number of particles (which remains constant, i.e. no

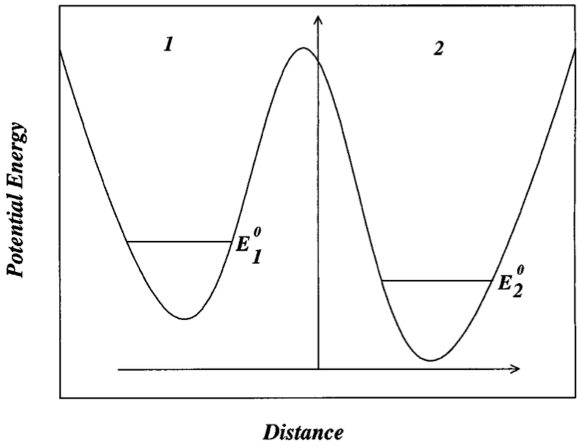

FIGURE 2.1. An example of a double well trap for a Bose-Einstein condensate. For $E_1^0 = E_2^0$, this is a symmetric trap. This figure is adapted from [**4**].

loss of particles) in the system. The interaction term κ depends on the strength of the barrier between the two wells. To place the particles in each of the wells, some energy needs to be put into the system; this is represented by the energies U_1 and U_2, with $U_1 N_1$ and $U_2 N_2$ the bulk on-site energies to place the entire population in the respective wells. The two condensates form a two-body coupled system where the dynamics are governed by (2.15) and (2.16) [**4**].

$$i\hbar \frac{\partial \psi_1}{\partial t} = \left(E_1^0 + U_1 N_1 \right) \psi_1 - \kappa \psi_2 \tag{2.15}$$

$$i\hbar \frac{\partial \psi_2}{\partial t} = \left(E_2^0 + U_2 N_2 \right) \psi_2 - \kappa \psi_1 \tag{2.16}$$

The one-body wavefunctions $\psi_{1,2}$ (2.17) are given in terms of the number of particles $N_{1,2}$ and the phase $\phi_{1,2}$

$$\psi_{1,2} = \sqrt{N_{1,2}} e^{i\phi_{1,2}} \tag{2.17}$$

We define the following two useful quantities:

$$z = \frac{N_1 - N_2}{N} \tag{2.18}$$

$$\varphi = \phi_1 - \phi_2 \tag{2.19}$$

A solution for the coupled Schrödinger equations ((2.15) and (2.16)) with (2.17) yields a condensed form for the rate of change of the population imbalance ($\dot{z}$) in 2.18 and the phase ($\dot{\varphi}$) in 2.21, in terms of ΔE (2.22) and Λ (2.23). Here, for mathematical simplicity, we have taken $\hbar = 1$ and remapped $2\kappa t \to t$.

$$\dot{z} = -\sqrt{1 - z^2} \sin \varphi \tag{2.20}$$

$$\dot{\varphi} = \Lambda z + \frac{z}{\sqrt{1 - z^2}} \cos \varphi + \Delta E \tag{2.21}$$

$$\Delta E = \frac{E_1^0 - E_2^0}{2\kappa} + N \frac{(U_1 - U_2)}{4\kappa} \tag{2.22}$$

$$\Lambda = N \frac{(U_1 + U_2)}{4\kappa} \tag{2.23}$$

With the above relations in our arsenal, we attain some remarkable conclusions for the case of an interacting nonlinear Bose gas. We carry out a numerical simulation for (2.20) and (2.21). We define the initial conditions ($t \to 0$) to be:

$$z(0) = 0.6$$

$$\varphi(0) = 0$$

Consider the case when $\Delta E \rightarrow 0$. In such a case (a symmetric double-well trap), $E_1^0 = E_2^0$, and Λ, which is a measure of the interaction strength of the two condensates through the barrier, is the useful parameter that governs the population imbalance z. In Figure 2.2, we observe pure sinusoidal oscillations for strong interactions ($\Lambda \rightarrow 1.0$). As the interaction strength is decreased ($\Lambda \rightarrow 8.0$), the oscillations become distorted. With increasing Λ, the oscillations around $z = 0$ gain an anharmonic character. As $\Lambda \rightarrow \Lambda_c = 10.0$, the oscillations approach a critical transition (Figure 2.3). Finally, as $\Lambda \rightarrow 12.0$, the population in each individual trap starts to oscillate at a non-zero time averaged value $\langle z(t) \rangle \neq 0$. This is the so-called *self-trapping effect.* This quantum non-linear tunneling effect is a consequence of the inter-atomic interaction in each of the wells.

In the self-trapping regime, this population imbalance, which always favors one of the two wells, perfectly showcases the distinction between the superconductive Josephson junction and the bosonic Josephson junction. In the former, charge imbalance is suppressed either by the inability of the junction to sustain an electric field, or by an external circuit which maintains a balanced charge across the junction.

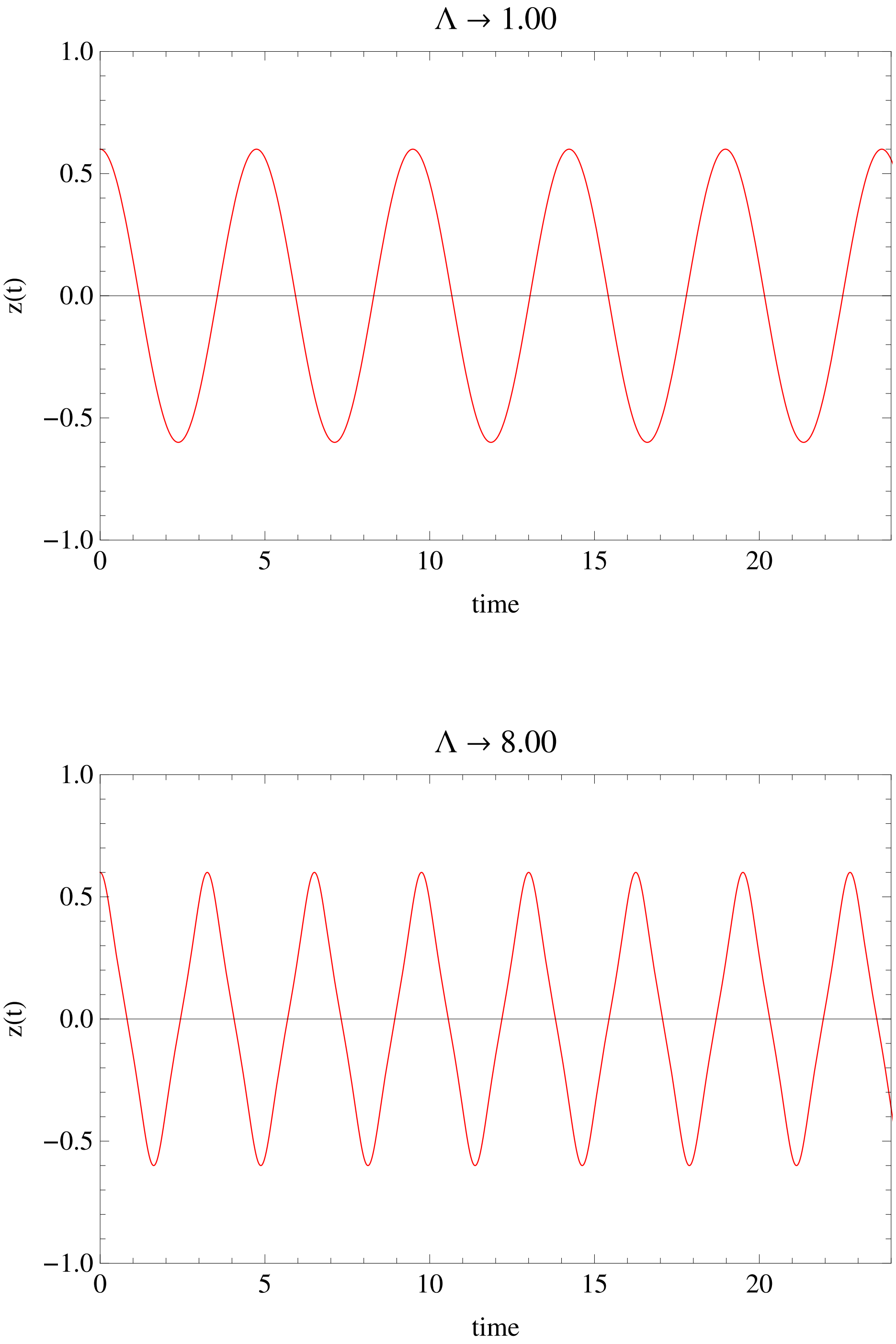

Figure 2.2. The fractional population imbalance $z(t)$ is plotted along the remapped time $2\kappa t$. We use the defined initial conditions and consider $\Lambda \in \{1, 8\}$.

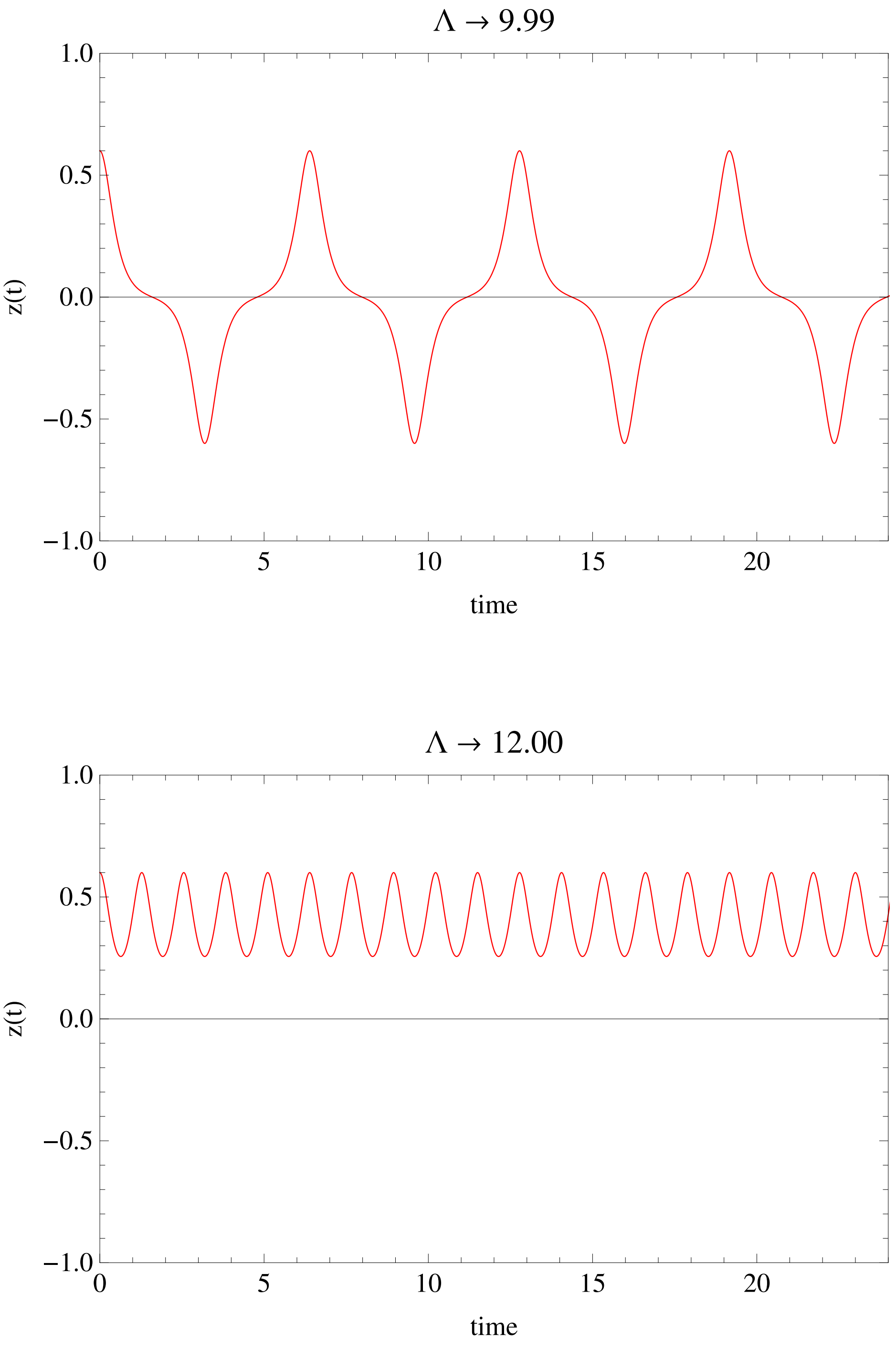

FIGURE 2.3. The fractional population imbalance $z(t)$ is plotted along the remapped time $2\kappa t$. We use the defined initial conditions and consider $\Lambda \in \{9.99, 12\}$.

Chapter 3

Quantum Dynamics in Two-Level Systems

Bose-Einstein condensates present to us a useful interactive system of atoms. In the previous chapter, we considered the Gross-Pitaeskii equation and studied how it laid out the theme for coupled condensates. In this chapter, we will consider a single system composed of multiple components (e.g. different spin states in a hyperfine manifold). We will discuss the coherent dynamics of a two-level system and the general formalism as applied to the goals of this thesis. We will start by considering a two-level system interacting with an electromagnetic field in the semi-classical formalism (Section 3.1). We will introduce the notion of coherence, and the role it plays in nonequilibrium dynamics of the Bose-Einstein condensate. To gain better insight into the behavior of different spin components in the condensate, we will transform our system to a rotating frame (Section 3.2) and adopt the rotating wave approximation. Section 3.3 will discuss the emergence of Rabi oscillations in our two-level system. This will enable us to better understand population dynamics between spin states.

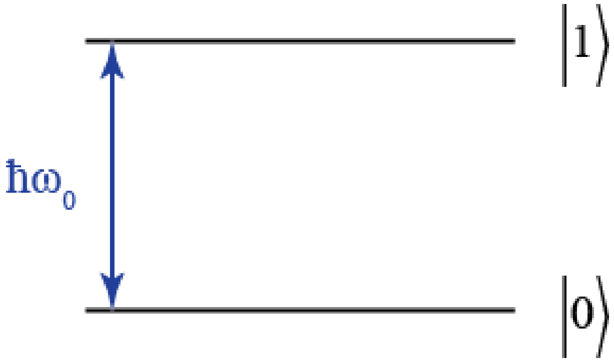

FIGURE 3.1. A representation of a two-level system. $|0\rangle$ and $|1\rangle$ represent the two eigenstates for the system, with $\hbar\omega_0$ the unperturbed energy difference between the two states.

3.1. The Two Level Atom

Two-level systems capture the quantum mechanics behind the ideas of magnetic trapping, and optical manipulation and detection. In this section, we will discuss the semi-classical dynamics (by considering a large number of photons) of a quantum two-level system in the presence of near-resonant electromagnetic radiation. This could be the spin states of an electron in the presence of microwave or radio-frequency radiation. Let us consider two energy levels $|0\rangle$ and $|1\rangle$ (Figure 3.1) where we will treat $|0\rangle$ as the ground state with some energy E_0, and $|1\rangle$ as the excited state with energy E_1. The energy $E_2 - E_1$ is given by $\hbar\omega_0$, and is the energy difference between the two bare states.

For such a two-level system, the resonant electromagnetic radiation has the angular frequency ω_0. $|0\rangle$ and $|1\rangle$ are the eigenstates of the bare Hamiltonian $\hat{H}_0$ without any driving field or perturbations. The eigenvalue of an eigenstate is the energy of that bare state:

$$\hat{H}_0 \left|0\right\rangle = E_0 \left|0\right\rangle = 0 \left|0\right\rangle$$

$$\hat{H}_0 \left|1\right\rangle = E_1 \left|1\right\rangle = \hbar\omega_0 \left|1\right\rangle$$

Now, let us consider the two-level system in the presence of an electromagnetic radiation field with angular frequency $\omega = \omega_0 + \Delta$ where Δ is the detuning of the field from the resonance of the bare states (Figure 3.2). For a system in the eigenstate $\left|i\right\rangle$ at time $t = 0$ with no phase, we can represent the phase evolution of the system with the factor of $\exp\left[\frac{-iE_i}{\hbar}t\right]$. In other words $\left|\psi(0)\right\rangle = \left|i\right\rangle \Rightarrow \left|\psi(t)\right\rangle = \left|i\right\rangle \exp\left[\frac{-iE_i}{\hbar}t\right]$. Then, the rate of change of $\left|\psi(t)\right\rangle$ is given as:

$$\begin{aligned}
\frac{d}{dt}\left|\psi(t)\right\rangle &= \frac{d}{dt}\left(\left|i\right\rangle \exp\left[\frac{-iE_i}{\hbar}t\right]\right) \\
&= -\frac{i}{\hbar}\exp\left[\frac{-iE_i}{\hbar}t\right] E_i \left|i\right\rangle \\
&= -\frac{i}{\hbar}\exp\left[\frac{-iE_i}{\hbar}t\right] \hat{H}_0 \left|i\right\rangle \\
\frac{d}{dt}\left|\psi(t)\right\rangle &= -\frac{i}{\hbar}\hat{H}_0 \left|\psi(t)\right\rangle \qquad (3.1)
\end{aligned}$$

We have obtained the general time-dependent Schrödinger equation [**31**], which means that $\psi(t)$, as we have defined it, is a valid quantum mechanical wavefunction. For such a system, when the entire population is in a single eigenstate, the state probability $P_i =$

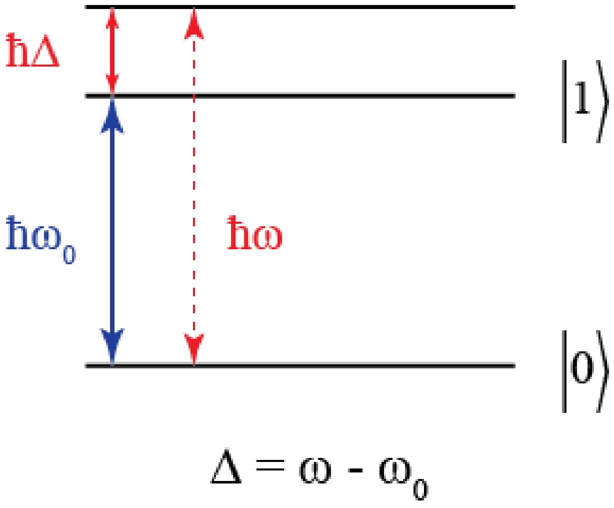

FIGURE 3.2. A representation of a two-level system in an electromagnetic field with the angular frequency $\omega = \omega_0 + \Delta$.

$|\langle i\,|\,\psi(t)\rangle|^2 = 1$. The major hallmark of quantum mechanics is the postulate that a single particle can be a in a superposition of states at some t. We assign state coefficients c_0 and c_1 to the bare eigenstates $|0\rangle$ and $|1\rangle$. This allows us to represent our system with a wavefunction $|\psi\rangle$ for our system (as given in Figure 3.2). The state coefficients obey the relation $|c_0|^2 + |c_1|^2 = 1$, and just as before, the probability of occupying a state is $|\langle i\,|\,\psi\rangle|^2 = |c_i|^2$ where $i \in \{1, 2\}$ for our two-level system.

$$|\psi\rangle = c_0\,|0\rangle + c_1\,|1\rangle \tag{3.2}$$

The bare Hamiltonian $\hat{H}_0$ in matrix formulation in the $\{|0\rangle, |1\rangle\}$ basis is given by (3.3). We can introduce a driving field, represented by a perturbation Hamiltonian $\hat{V}$ to couple the two eigenstates and drive transitions between them. The driving field induces a dipole moment between the two states, which leads to an oscillatory perturbation upon its interaction with the electromagnetic field. For this reason, $\hbar\Omega = \mu E_0$ where μ is the induced dipole in the particles and E_0 is the amplitude of the electromagnetic field. Here we treat the Rabi frequency Ω as a completely real driving frequency, so that $\Omega^* = \Omega$. We also assume that the phase delay associated with the driving field $\phi_V \to 0$ so that $\cos(\omega t + \phi_V) \to \cos \omega t$

$$\hat{H}_0 = \hbar \begin{pmatrix} 0 & 0 \\ 0 & \omega_0 \end{pmatrix} \tag{3.3}$$

$$\hat{V} = \hbar \begin{pmatrix} 0 & \Omega \cos \omega t \\ \Omega \cos \omega t & 0 \end{pmatrix} \tag{3.4}$$

Then, the effective Hamiltonian of the system $\hat{H_{eff}}$ is obtained by adding $\hat{H}_0$ and $\hat{V}$ (3.5). Note that coupling the two states means that $|0\rangle$ and $|1\rangle$ are no longer the stationary states of the system.

$$\hat{H}_{eff} = \hbar \begin{pmatrix} 0 & \Omega \cos \omega t \\ \Omega \cos \omega t & \omega_0 \end{pmatrix} \tag{3.5}$$

3.2. The Interaction Picture

In order to better grasp the consequences of (3.5), we note that, as it stands $\hat{H}_{eff}$ is time dependent. To remove the time-dependence, the Hamiltonian can be viewed in the interaction picture (also known as the rotating frame). Here, we present a concise version of the transformation technique, which is a purely mathematical procedure.

Let us define the unitary operator $\hat{U} = e^{\left[-i\hat{H}_1 t/\hbar\right]}$ and the Hermitian operator $\hat{H}_1$ (3.6). Then, we transform our system $|\psi\rangle \to \left|\tilde{\psi}\right\rangle$.

$$\hat{H}_1 = \hbar \begin{pmatrix} 0 & 0 \\ 0 & \omega \end{pmatrix} \tag{3.6}$$

$$\widetilde{|\psi\rangle} = \hat{U}^* \, |\psi\rangle \tag{3.7}$$

Then (3.8) is a direct consequence of (3.6) (from the Appendix). The Hamiltonian $\hat{H}_{RF}$ applies in the interaction picture or the rotating frame (RF)[1]

$$\hat{H}_{RF} = \hat{U}^* \left(\hat{H}_{eff} - \hat{H}_1 \right) \hat{U} \tag{3.8}$$

We should restate the effective Hamiltonian $\hat{H}_{eff}$ in an exponential form before we transform to the rotating frame (3.9).

$$\hat{H}_{eff} = \frac{\hbar}{2} \begin{pmatrix} 0 & \Omega \left(e^{i\omega t} + e^{-i\omega t} \right) \\ \Omega \left(e^{i\omega t} + e^{-i\omega t} \right) & 2\omega_0 \end{pmatrix} \tag{3.9}$$

Employing (3.9) and (3.8), we obtain (3.10) for the Hamiltonian matrix in the interaction picture.

$$\begin{aligned} \hat{H}_{RF} &= \hat{U}^* \left(\hat{H}_{eff} - \hat{H}_1 \right) \hat{U} \\ &= e^{\left[i\hat{H}_1 t/\hbar \right]} \frac{\hbar}{2} \left[\begin{pmatrix} 0 & \Omega \left(e^{i\omega t} + e^{-i\omega t} \right) \\ \Omega \left(e^{i\omega t} + e^{-i\omega t} \right) & 2\omega_0 \end{pmatrix} - \begin{pmatrix} 0 & 0 \\ 0 & 2\omega \end{pmatrix} \right] e^{\left[-i\hat{H}_1 t/\hbar \right]} \end{aligned}$$

---

[1] For purposes of this thesis, the abbreviation RF is used to refer to the 'rotating frame' and should not be confused with radio-frequency, which is also sometimes denoted in several articles as RF.

$$\begin{aligned}\hat{H}_{RF} &= \frac{\hbar}{2}\begin{pmatrix}1 & 0\\ 0 & e^{i\omega t}\end{pmatrix}\begin{pmatrix}0 & \Omega\left(e^{i\omega t}+e^{-i\omega t}\right)\\ \Omega\left(e^{i\omega t}+e^{-i\omega t}\right) & 2\left(\omega_0-\omega\right)\end{pmatrix}\begin{pmatrix}1 & 0\\ 0 & e^{-i\omega t}\end{pmatrix}\\ &= \frac{\hbar}{2}\begin{pmatrix}0 & \Omega\left(1+e^{-i2\omega t}\right)\\ \Omega\left(1+e^{i2\omega t}\right) & -2\Delta\end{pmatrix}\end{aligned} \tag{3.10}$$

At this point, we invoke the *rotating wave approximation* which allows us to drop the exponential terms since they oscillate at twice the driving frequency 2ω. Finally, we obtain a simplified time independent form for the Hamiltonian $\hat{H}'$ given in (3.11). We can use this Hamiltonian and the Schrodinger equation (3.1) to find the evolution of the state amplitudes for the new states.

$$\hat{H}' = \frac{\hbar}{2}\begin{pmatrix}0 & \Omega\\ \Omega & -2\Delta\end{pmatrix} \tag{3.11}$$

3.3. Rabi Oscillations in a Two-Level Atom

In (3.11) we have a Hamiltonian describing the behavior of a quantum mechanical two-level system whose original states $|0\rangle$ and $|1\rangle$ are no longer stationary states. The new states in the interaction picture can be thought of as states on the Bloch sphere. Usually the states gain phase as they evolve with time, now we move to the frame where they are stationary. Note that from (3.7) it follows that the state probabilities continue to be $\left|\left\langle \hat{U}^* i \,\middle|\, \psi \right\rangle\right|^2 = |c_i|^2$ for $i \in \{1,2\}$ states.

To probe into the consequences of $\hat{H}'$ on the state amplitudes, the Schrödinger equation (3.1) is used to find the rate of change of state amplitudes of $\left|\widetilde{\psi}(t)\right\rangle$.

$$i\hbar\frac{d}{dt}\left|\widetilde{\psi}(t)\right\rangle = \hat{H}'\left|\widetilde{\psi}(t)\right\rangle$$

Continuing our use of the state basis, in matrix form this is (3.12):

$$i\hbar\begin{pmatrix}\dot{c_0}(t)\\ \dot{c_1}(t)\end{pmatrix} = \frac{\hbar}{2}\begin{pmatrix}0 & \Omega\\ \Omega & -2\Delta\end{pmatrix}\begin{pmatrix}c_0(t)\\ c_1(t)\end{pmatrix} \tag{3.12}$$

An alternate method is to restate this as a system of coupled differential equations. We start with the entire population in the RF state corresponding to $|0\rangle$, i.e. $c_0(t=0)=1$.

$$\begin{aligned}
2i\dot{c_0}(t) &= \Omega c_1(t)\\
2i\dot{c_1}(t) &= \Omega c_0(t) - 2\Delta c_1(t)\\
c_0(0) &= 1\\
c_1(0) &= 0
\end{aligned} \tag{3.13}$$

The state probabilities $c_0(t)$ and $c_1(t)$ evolve as given in (3.14). Here, we have replaced the angular frequency term $\sqrt{\Omega^2+\Delta^2}$ with Ω_R. Ω_R is known as the *total Rabi frequency* for this two-level system. As $\Delta \to 0, \Omega_R \to \Omega$ (the Rabi frequency), which is the case where the electromagnetic field is in resonance with the energy separation between the two levels (consider figure 3.2 when $\Delta = 0$)

$$\begin{pmatrix} c_0(t) \\ c_1(t) \end{pmatrix} = e^{\dfrac{i\Delta t}{2}} \begin{pmatrix} \cos\left(\dfrac{\Omega_R t}{2}\right) - \dfrac{i\Delta}{\Omega_R}\sin\left(\dfrac{\Omega_R t}{2}\right) \\ -\dfrac{i\Omega}{\Omega_R}\sin\left(\dfrac{\Omega_R t}{2}\right) \end{pmatrix} \tag{3.14}$$

Any experiment with such a two-level system (e.g. electron with spin states interacting with a microwave or radio-frequency field) will produce observations of the quantities $|c_i|^2$ (3.15) and (3.16), where $|i\rangle$ is a state of the system under consideration. Ω_R (total Rabi frequency) is the frequency of oscillation of the state probabilities.

$$|c_0(t)|^2 = \frac{\Delta^2}{\Omega_R^2} + \frac{\Omega^2}{\Omega_R^2}\cos^2\left(\frac{\Omega_R t}{2}\right) \tag{3.15}$$

$$|c_1(t)|^2 = \frac{\Omega^2}{\Omega_R^2}\sin^2\left(\frac{\Omega_R t}{2}\right) \tag{3.16}$$

In what follows we will consider the case of an on-resonance electromagnetic field ($\Delta \to 0$) and a slightly detuned electromagnetic field ($\Delta \neq 0$).

3.3.1. On-Resonance Field

The first case we will consider is that when the electromagnetic field is on resonance with the energy level separation between the $|0\rangle$ and $|1\rangle$. As $\Delta \to 0$,$\omega = (\omega_0 + \Delta) \to \omega_0$. In this case, the probability dynamics of the states, (3.15) and (3.16), can be simplified to yield equations (3.17) and (3.18).

$$|c_0(t)|^2 \overset{\Delta=0}{\Longrightarrow} \cos^2\left(\frac{\Omega t}{2}\right) \tag{3.17}$$

$$|c_1(t)|^2 \overset{\Delta=0}{\Longrightarrow} \sin^2\left(\frac{\Omega t}{2}\right) \tag{3.18}$$

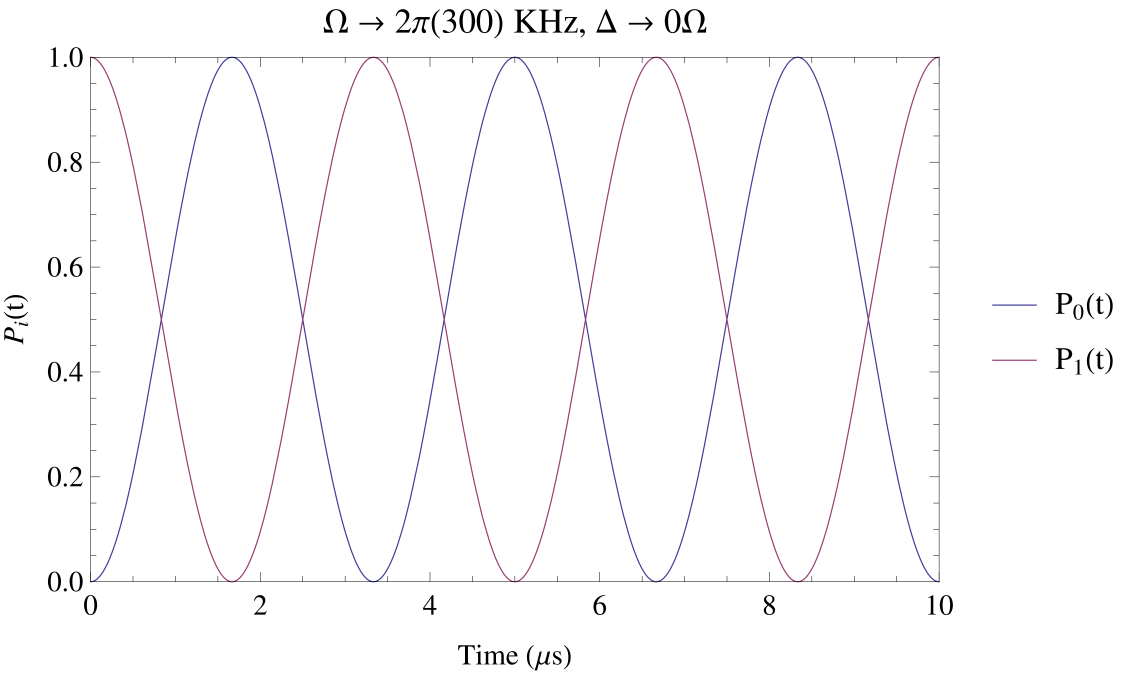

FIGURE 3.3. Rabi Oscillations in a two-level system at $\frac{\Omega_R}{2\pi} \rightarrow \frac{\Omega_R}{2\pi} = 300$ KHz.

We present Rabi oscillations of the state probabilities $P_0 = |c_0(t)|^2$ and $P_1 = |c_1(t)|^2$ in the quantum mechanical two-level system in Figure 3.3 . In this case, we note that as $t \rightarrow 1.7\mu s$, $P_0 \rightarrow 0$ and $P_1 \rightarrow 1$. Such a pulse that entirely transforms the state of the system is known as the π-pulse. Similarly, a pulse time of say, $3.4\mu s$ represents the time it takes to for the system to return to its starting point. We refer to such a pulse as a 2π-pulse, and the time of a 2π-pulse is the period of the Rabi oscillations. The oscillation frequency is Ω, and therefore the 2π-pulse time is dictated by the total Rabi frequency.

3.3.2. Off-Resonance Field

Let us now consider the case when the electromagnetic field is slightly detuned from the resonance, i.e. $\Delta \rightarrow \alpha\Omega$. In this case, the general equations (3.15) and (3.16) are used to examine the population dynamics of the two states. We consider the case when $\alpha \in \{0.4, 1.0, 4.0\}$ (Figure 3.4).

As Δ increases, the amplitude of Rabi oscillations decreases. The period of the oscillations decreases because the *total Rabi frequency*, $\Omega_R = \sqrt{\Omega^2 + \Delta^2}$ increases even though the Rabi frequency $\Omega/2\pi = 300$ KHz stays constant. At a high value for the detuning ($\Delta \to 4\Omega$), we see that the Rabi oscillations die out and the state probabilities approach a limit. In other words, the time-average value $\langle P_i(t) \rangle \to P_i(t = 0)$ (this is seen in the bottom plot in Figure 3.4).

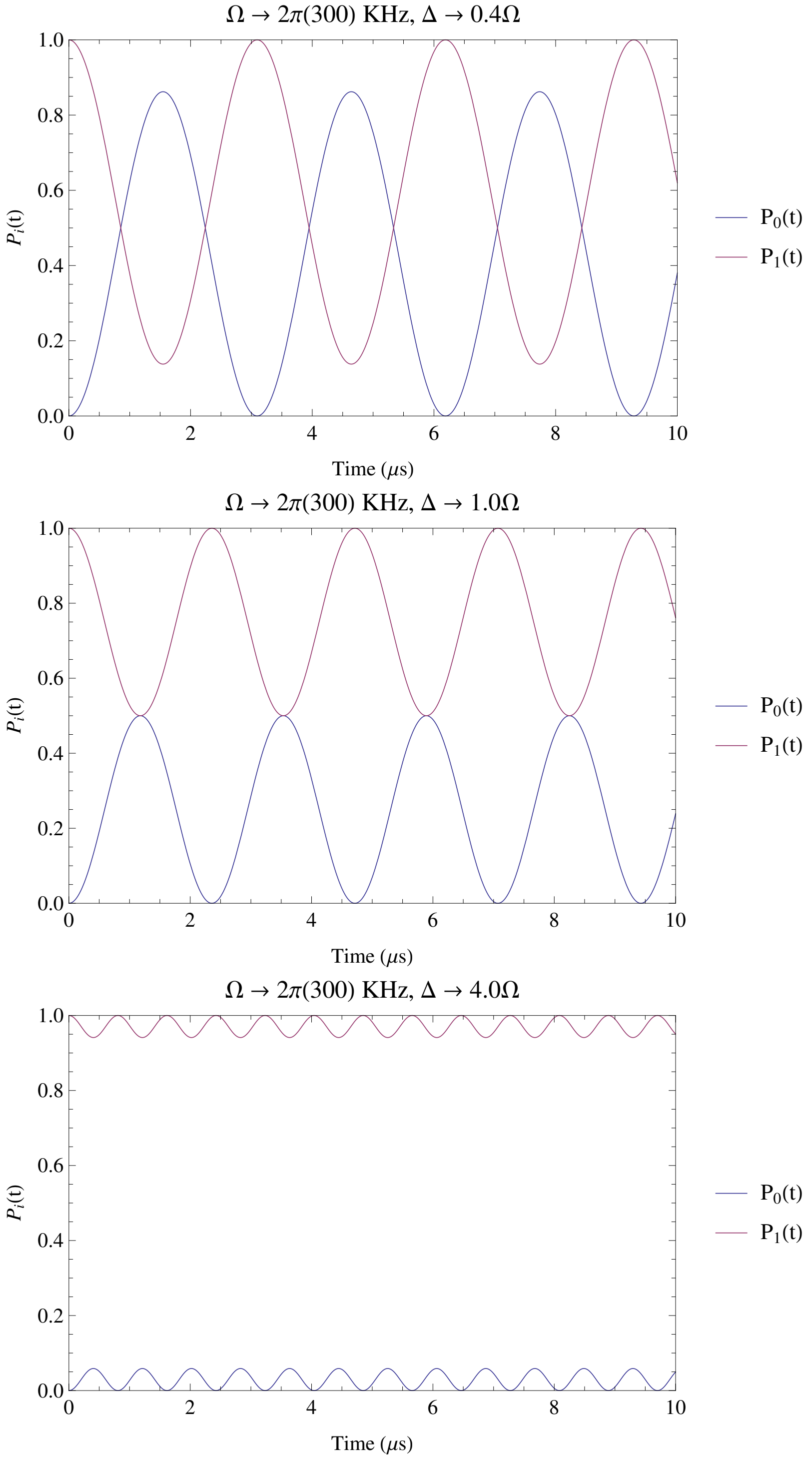

FIGURE 3.4. A plot of the Rabi oscillations (P_i)for a two-level system, plotted as a function of time for the states $i \in \{0, 1\}$. Here, we have plotted oscillations for the case of $\Delta \in \{0.4\Omega, 1.0\Omega, 4.0\Omega\}$. The oscillations die out at high values of the detuning from the resonance.

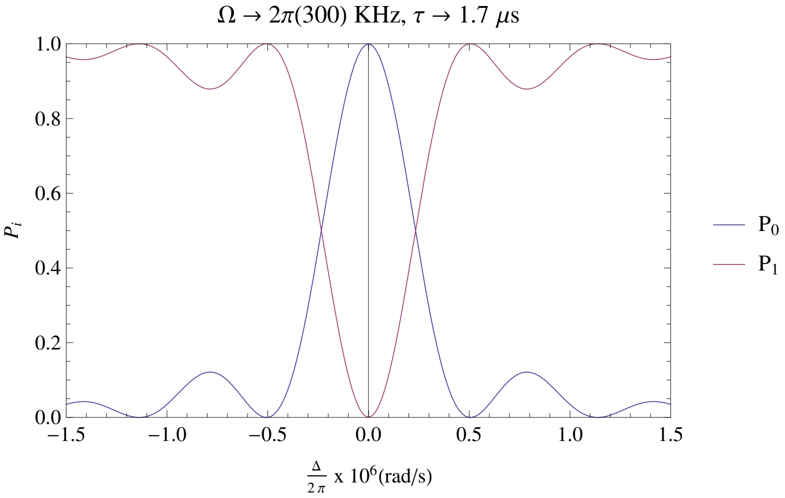

FIGURE 3.5. A representation of $P_i(\omega - \omega_0)$ at $\frac{\Omega}{2\pi} = 300$ KHz with a pulse time of 1.7 μs. In the Fourier domain, the state amplitudes display sinc-like behavior.

3.3.3. Rabi Oscillations in Fourier Space

In order to better grasp the effect of Δ on the state amplitudes, we can carry out an analysis in the Fourier (or frequency) domain instead of the time domain. We pick a specific pulse time (a π-pulse time is an obvious choice, since at $\Delta \to 0$, one of the states will have the probability $P_i(\omega = \omega_0) = 1$ while the other state will remain empty), and predict the population dynamics as a function of Δ.

We see from Figure 3.5 that at $\Delta \to 0$, $P_0 \to 1$. This is because we have chosen the pulse time to be 1.7 μs, which also happens to be the π-pulse time for $\frac{\Omega}{2\pi} \to 300$ KHz. At high values of detuning, the oscillations die out, and $\tau \to 1.7\ \mu s$ fails to be the π-pulse for the system. This is obvious from figure 3.5 since a pulse time of $\tau \to 1.7\ \mu s$ does not convert the entire population from P_1 to P_2 (recall that this is how a π-pulse is defined).

Chapter 4

The Rubidium-87 Atom: A Three-Level System

The ^{87}Rb alkali atom presents to us numerous multi-level quantum mechanical systems. In our lab, we use the $D2$ transitions to cool down the atoms in the laser cooling process. The $D2$ line represents the transitions between the quantum mechanical energy levels $5^2S_{1/2}$ and $5^2P_{3/2}$ (Figure 1.3), which have a wavelength gap in the near-infrared range of the electromagnetic spectrum at about 780.24 nm.

As the condensate forms, the bosons are in the ground state $5^2S_{1/2}$. In the ground state, we have access to the hyperfine levels $F = 1$ and $F = 2$. In the presence of an external magnetic field, the hyperfine levels split up into $(2F + 1)$ zeeman sublevels. As a result, the $F = 1$ hyperfine level now represents a three-level system ($m_F \in \{-1, 0, 1\}$) while the $F = 2$ hyperfine level is essentially a five-level system ($\{-2, -1, 0, 1, 2\}$). Based on the laser cooling techniques adapted and the long-term goals, ultra-cold atomic labs may find it easier to work with the atoms in one of the two hyperfine levels. In our lab, we employ a magnetic dipole trap to hold the atoms after the evaporative cooling stage; we trap the bosons in the $|F = 1, m_F = -1\rangle$ hyperfine state. This provides us with a neat three-level ladder system to study the non-equilibrium dynamics, especially the Rabi oscillations, displayed by the condensate.

In this chapter, we start by introducing the three-level system, and considering the Hamiltonian for this particular configuration in Section 4.1. We then examine the system in the interaction picture, and invoke the rotating wave approximation. Predictions for the evolution of the state probabilities are presented in Section 4.2. For the on-resonance driving field, we compare our experimental results with the theoretical predictions to determine the effective parameters governing our system. Then, we consider the case of an off-resonant electromagnetic field. We state the Rabi dynamics for $\Delta \neq 0$, before a comparison with the acquired experimental data is produced. Finally, we explore the possible causes for the shift of the resonance at strong driving field frequency Ω.

4.1. The Zeeman Three-Level Ladder System

The $F = 1$ hyperfine manifold of the $5^2S_{1/2}$ state in ^{87}Rb has a degeneracy of 3. In the presence of an external magnetic field, this degeneracy is lifted and the hyperfine level splits into the three Zeeman states. The energies of the levels and their splitting is determined by the strength of the B-field. This non-linear behavior is depicted by the Breit-Rabi formula (refer to Section 1.3).

At weak magnetic field strengths, the energy separations between the three levels can be approximated as equal (4.1). As showcased by the Breit-Rabi formula, this approximation does not apply in the strong B-field regime, where the splitting gains a quadratic character. In our apparatus, the dipole trap has $B \approx 5.5G$, which places us in the linear weak field regime. This corresponds to a resonant frequency of $\omega_0 \approx 3.85$ x 10^6 rad s^{-1} at weak values of the driving field.

$$E_{|1,1\rangle} - E_{|1,0\rangle} \approx E_{|1,0\rangle} - E_{|1,-1\rangle} = \hbar\omega_0 \tag{4.1}$$

The three-level system (Figure 4.1) is radio-frequency coupled, which shows up as the parameter $\Omega \cos wt$ in the effective Hamiltonian. The radio-frequency of angular frequency ω is generated with the use of an antenna. Here the energy spacing is $\hbar\omega_0$ and then the three levels represent the Zeeman sublevels of the $F = 1$ ground state of Rubidium.

$$|0\rangle : |F = 1, m_F = -1\rangle$$

$$|1\rangle : |F = 1, m_F = \ 0\rangle$$

$$|2\rangle : |F = 1, m_F = +1\rangle$$

The system is represented with the wavefunction $|\psi\rangle$ which is defined in terms of the eigenstates and the state coefficients c_i for $i \in \{0, 1, 2\}$ (4.2).

$$|\psi\rangle = c_0 |0\rangle + c_2 |1\rangle + c_2 |2\rangle \tag{4.2}$$

We define the Hamiltonian $\hat{H}_0$ for this three-level system with only two non-zero diagonal elements (4.3). Here we have treated the quantum level $|0\rangle$ as the ground state level with energy $E_0 = 0$ [1]. In this way, the eigenvalues of the states are the energies of the

---

[1] A non-zero ground energy adds a constant bias to the Hamiltonian and does not affect the state dynamics.

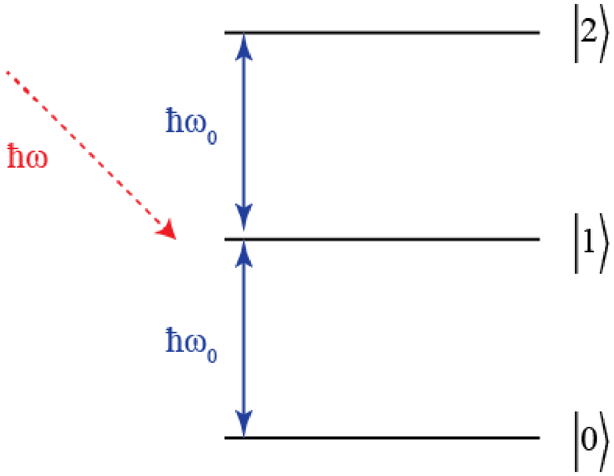

FIGURE 4.1. The Zeeman three-state system for ^{87}Rb. With a radio-frequency field (angular frequency ω), the system behaves as a coupled three-level system. The Zeeman splitting between the three levels is taken to be the same ($\hbar\omega_0$) in this weak Zeeman field regime.

eigenstates.

$$\hat{H}_0 = \hbar \begin{pmatrix} 0 & 0 & 0 \\ 0 & \omega_0 & 0 \\ 0 & 0 & 2\omega_0 \end{pmatrix} \tag{4.3}$$

$$\hat{H}_0 |0\rangle = 0 |0\rangle$$

$$\hat{H}_0 |1\rangle = \hbar\omega_0 |1\rangle$$

$$\hat{H}_0 |2\rangle = 2\hbar\omega_0 |2\rangle$$

The driving field results in an oscillatory time-dependent perturbation V (4.4) represented by the factor $\cos\omega t$. The ladder arrangement of the quantum levels means that the states $|0\rangle$ and $|2\rangle$ are coupled to the middle state $|1\rangle$ (which is coupled to both of the outer states $|0\rangle$ and $|2\rangle$). Here we have assumed that the driving field does not have a phase association with it, so that $\Omega = \Omega^*$.

$$\hat{V} = \hbar \begin{pmatrix} 0 & \Omega \cos \omega t & 0 \\ \Omega \cos \omega t & 0 & \Omega \cos \omega t \\ 0 & \Omega \cos \omega t & 0 \end{pmatrix} \tag{4.4}$$

The effective Hamiltonian $\hat{H}_{eff}$ is the sum of the internal and the perturbation Hamiltonians (4.5). The coupling means that the eigenstates $|i\rangle$ are no longer the stationary states. In fact, the time-dependence means that there are no *stationary* states for this system (at least in the current lab frame).

$$\hat{H}_{eff} = \hbar \begin{pmatrix} 0 & \Omega \cos \omega t & 0 \\ \Omega \cos \omega t & \omega_0 & \Omega \cos \omega t \\ 0 & \Omega \cos \omega t & 2\omega_0 \end{pmatrix} \tag{4.5}$$

In our search for the new states, we examine the system in the interaction picture by defining the new wavefunction $\left|\tilde{\psi}\right\rangle = \hat{U}^* |\psi\rangle$ where $\hat{U} = e^{-\frac{i\hat{H}_1 t}{\hbar}}$ is a unitary operator. Then, $\hat{H}_1$ must be a Hermitian operator (4.6).

$$\hat{H}_1 = \hbar \begin{pmatrix} 0 & 0 & 0 \\ 0 & \omega & 0 \\ 0 & 0 & 2\omega \end{pmatrix} \tag{4.6}$$

In the rotating frame, the new Hamiltonian $\hat{H}'$ (from Appendix) is found by computing:

$$\hat{H}' = \hat{U}^* \left[\hat{H}_0 - \hat{H}_1\right] \hat{U} \tag{4.7}$$

For the three-level effective Hamiltonian (4.5), the Hamiltonian in the interaction picture is time-independent (4.8), where $\Delta = (\omega - \omega_0)$. We have taken the *rotating wave approximation* which allows us to ignore terms oscillating at twice the driving frequency i.e. 2ω.

$$\hat{H}' = \frac{\hbar}{2}\begin{pmatrix} 0 & \Omega & 0 \\ \Omega & -2\Delta & \Omega \\ 0 & \Omega & -4\Delta \end{pmatrix} \tag{4.8}$$

4.2. Evolution of the State Probabilities

Now that we are in possession of a time-independent Hamiltonian (4.8), we apply Schrödinger's equation (4.9) to find the state dynamics.

$$\frac{d}{dt}\left|\tilde{\psi}\right\rangle = -\frac{i}{\hbar}\hat{H}'\left|\tilde{\psi}\right\rangle \tag{4.9}$$

Substituting (4.2) and (4.8) in (4.9), we can express the Schrödinger equation in matrix form (4.10).

$$i\hbar\begin{pmatrix} \dot{c_0}(t) \\ \dot{c_1}(t) \\ \dot{c_2}(t) \end{pmatrix} = \frac{\hbar}{2}\begin{pmatrix} 0 & \Omega & 0 \\ \Omega & -2\Delta & \Omega \\ 0 & \Omega & -4\Delta \end{pmatrix}\begin{pmatrix} c_0(t) \\ c_1(t) \\ c_2(t) \end{pmatrix} \tag{4.10}$$

This is essentially a system of three coupled differential equations, where $c_1(t)$ is coupled to both $c_0(t)$ and $c_2(t)$ while $c_0(t)$ and $c_2(t)$ are each coupled only to $c_1(t)$. We define the initial conditions such that the entire population of the system is in one of the three states.

$$\begin{aligned}
2i\dot{c}_0(t) &= \Omega c_1(t) \\
2i\dot{c}_1(t) &= \Omega c_0(t) - 2\Delta c_1(t) \\
2i\dot{c}_2(t) &= \Omega c_1(t) - 4\Delta c_2(t) \\
c_0(0) &= 1 \\
c_1(0) &= 0 \\
c_2(0) &= 0
\end{aligned} \tag{4.11}$$

Let us now enforce certain conditions on the system. In what follows, we will pay close attention to the two specific cases, namely the on-resonant case ($\Delta = 0$) and the general off-resonant case ($\Delta \neq 0$)

4.2.1. Resonant Driving Frequency

In the case of a resonant driving field, $\omega = \omega_0$ and $\Delta \to 0$. This means that the terms with Δ in the interaction Hamiltonian $\hat{H}'$ (4.8) go to zero. $\hat{H}'$ is essentially reduced to (4.12).

$$\hat{H}' = \frac{\hbar}{2}\begin{pmatrix} 0 & \Omega & 0 \\ \Omega & 0 & \Omega \\ 0 & \Omega & 0 \end{pmatrix} \tag{4.12}$$

Consequently, the system of differential equations (4.11) are simplified to yield 4.13

$$
\begin{aligned}
2i\dot{c_0}(t) &= \Omega c_1(t) \\
2i\dot{c_1}(t) &= \Omega c_0(t) \\
2i\dot{c_2}(t) &= \Omega c_1(t) \\
c_0(0) &= 1 \\
c_1(0) &= 0 \\
c_2(0) &= 0
\end{aligned} \tag{4.13}
$$

For such a coupled system, we obtain the dynamic state amplitude equations:

$$
\begin{pmatrix} c_0(t) \\ c_1(t) \\ c_2(t) \end{pmatrix} = \begin{pmatrix} \frac{1}{2}\left(\cos\frac{\Omega t}{\sqrt{2}} - 1\right) \\ -\frac{i}{\sqrt{2}}\sin\left(\frac{\Omega t}{\sqrt{2}}\right) \\ \frac{1}{2}\left(\cos\frac{\Omega t}{\sqrt{2}} + 1\right) \end{pmatrix} \tag{4.14}
$$

We present a theoretical plot of the state probabilities $|c_i(t)|^2$ for $i \in \{0, 1, 2\}$ in Figure 4.2. We predict that the state amplitudes $P_0(t) = |c_0(t)|^2$ and $P_2(t) = |c_2(t)|^2$ are related such that they are reflections about the line $P(t) = 0.5$, and have the same total Rabi frequency. There is a phase offset of half the oscillation period between $P_0(t)$ and $P_2(t)$. The population in the middle state, i.e. $P_1(t) = |c_1(t)|^2$ oscillates twice as fast compared to the other two quantum states. We also note the following results:

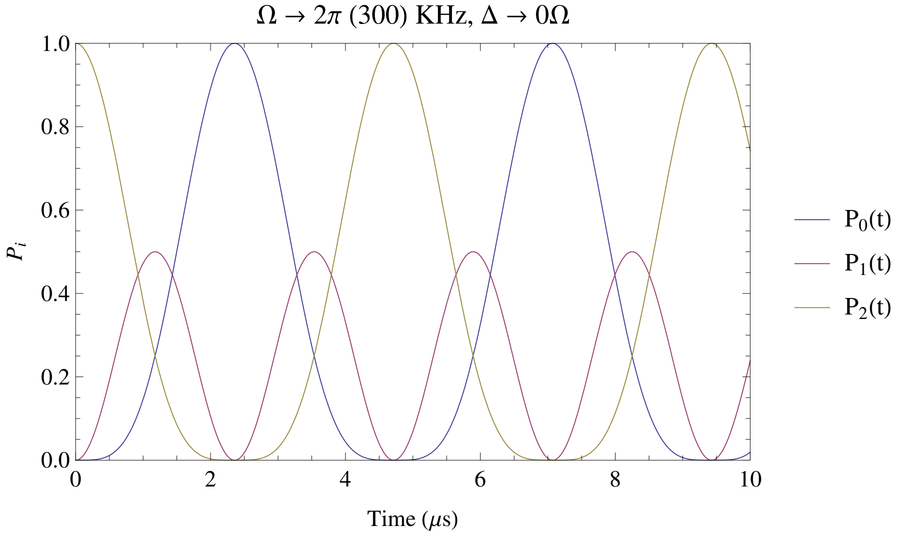

FIGURE 4.2. A plot of the Rabi oscillations for the three-level system. This is the case of $\Delta \to 0$.

$$0 \leq |c_0(t)|^2 \leq 1.0$$

$$0 \leq |c_1(t)|^2 \leq 0.5$$

$$0 \leq |c_2(t)|^2 \leq 1.0$$

In our laboratory setting, the Rabi frequency Ω is indirectly controlled by varying the power (in units of dBm)to an amplifier. This means that we can set a particular power input to our amplifier, and then record the Rabi oscillations displayed by the condensate. This experimental evidence not only showcases the Rabi profiles, but enables us to fit our analytical models to the data points and obtain a result for the Rabi frequency output of the amplifier. Here is our experimental data for Rabi oscillations ($\Delta \to 0$) at various amplifier input powers. It is important to note that ω is not the same for all the trials. This refers to the observed shift of the resonance in our experiments (more on this later).

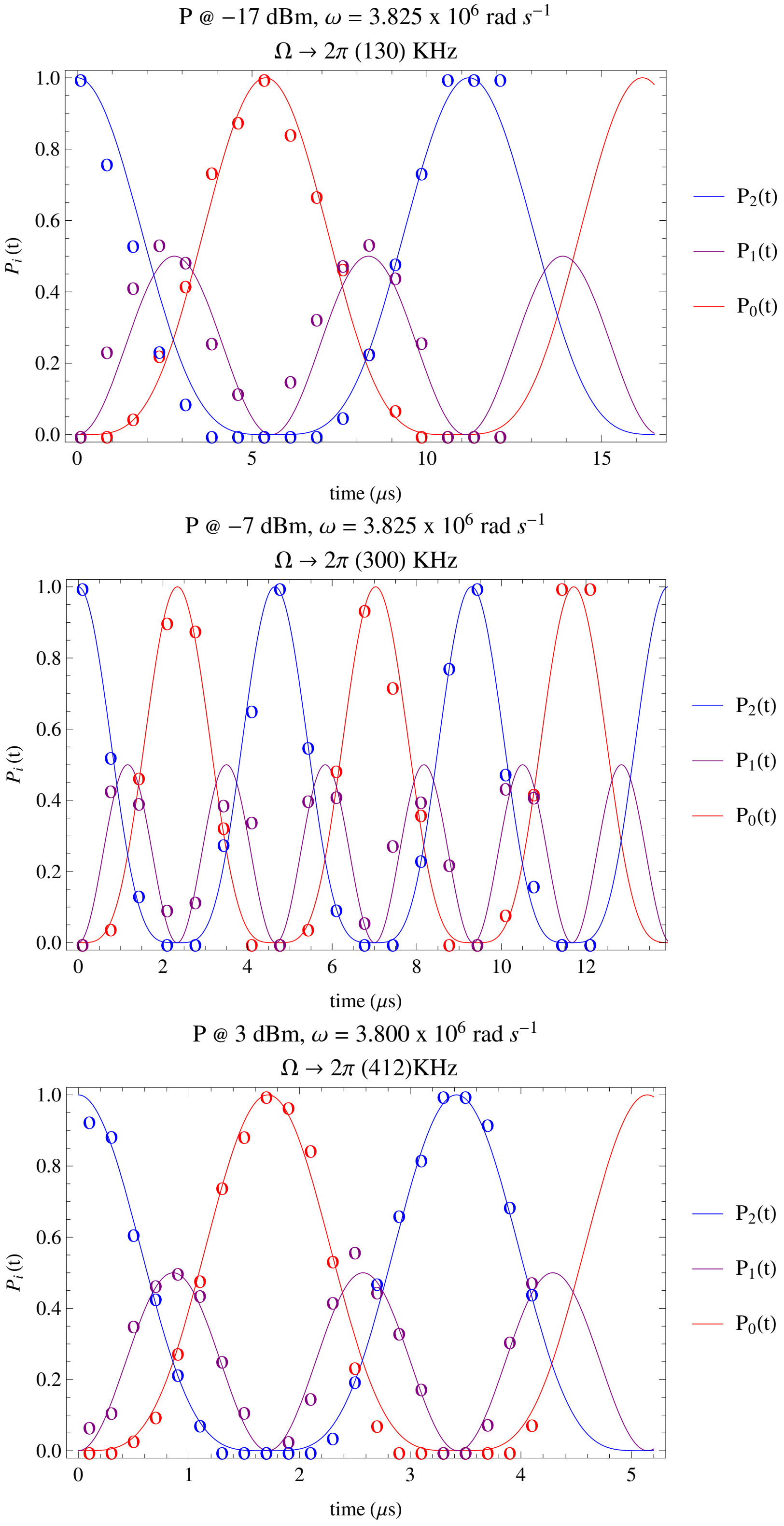

FIGURE 4.3. The data points represent the observed Rabi oscillations in the Zeeman sublevels of the ^{87}Rb atom ground state. The fitted models (curves) depict the behavior of the three Zeeman states in our laboratory. The corresponding Rabi frequency, Ω is found, and presented for each trial.

4.2.2. Off-Resonant Driving Frequency: The Fourier Domain

For a non-zero Δ, the system of coupled differential equations (4.11) needs to be solved analytically. This leads to a third-order differential equation with complex coefficients. The system can be solved with the defined initial conditions for a specified value for Δ. We plot the probabilities $P_i(t) = |c_i(t)|^2$ for $i \in \{0, 1, 2\}$ for $\Delta \in \{0.2\Omega, 0.5\Omega, 1.0\Omega\}$ in Figure 4.4.

We see that the clean Rabi oscillations have been affected by the detuning. The *total Rabi frequency* of the system increases with the magnitude of the detuning while the amplitude of the oscillations decreases. The population in the middle level $|1\rangle$ oscillates at twice the frequency of the other two states, with a smaller amplitude. In the limit, $\Delta \to \alpha\Omega$ where α is a comparatively larger number, the oscillations die out. This is depicted in Figure 4.5 for $\Delta \to 4.0\Omega$.

The effect of Δ on the state amplitudes can be better understood in Fourier space. In what follows, we vary the frequency ω instead of the radio-frequency pulse time. Fixing the pulse time, $t \to \tau$ where τ is the pulse time corresponding to a π-pulse. For a three-level system, the π-pulse is the radio-frequency pulse that converts the entire population from one of the two outer states $|0\rangle$ or $|2\rangle$ to the other one of the two. Similarly, a 2π-pulse represents a pulse time that makes the system complete a whole period of oscillation and return to the initial values. This creates the possibility of using multiple pulse times to attain the same final probability $P_i(t)$ for some $i \in \{0, 1, 2\}$ (4.15), where n is an integer.

$$P_i(\tau) = P_i(\tau + (2\tau)n) \tag{4.15}$$

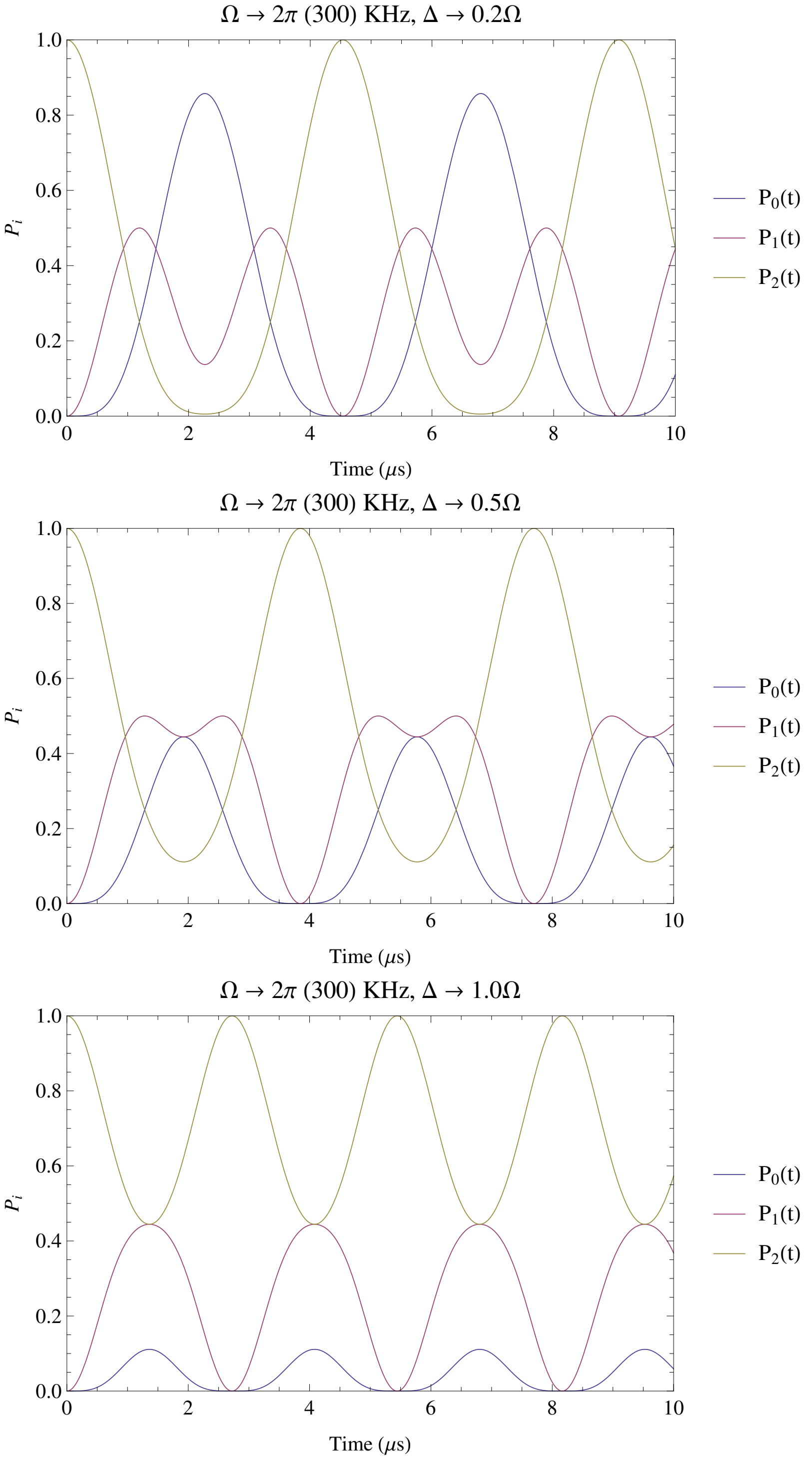

FIGURE 4.4. Here we present the evolution of the state probabilities for $\Omega \rightarrow 2\pi(300)$KHz. The three plots show dynamics for $\Delta \in \{0.2\Omega, 0.5\Omega, 1.0\Omega\}$.

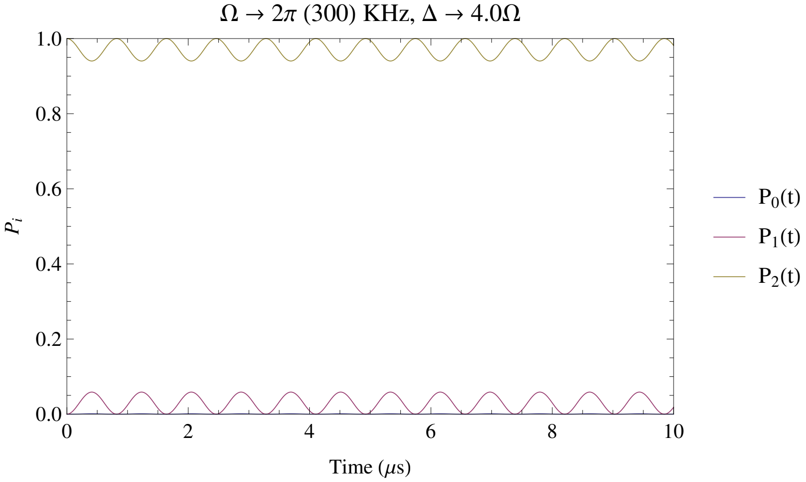

FIGURE 4.5. In this plot for $P_i(t)$ for $\Delta \rightarrow 4.0\Omega$, the oscillations die out and there are effectively no significant Rabi oscillations. This is the far-off resonant regime.

The state populations behave as *sinc* curves. Since the fourier domain and the time domain are inversely related, a longer pulse time corresponds to a narrower peak width in the fourier domain (as illustrated in Figure 4.6).

A typical theoretical plot of $P_i(\omega)$ for $i \in \{0, 1, 2\}$ and a fixed pulse time τ looks like the plots in Figure 4.6. Since the *total Rabi frequency* and π-pulse time are dependent upon the detuning, we see that $P_i(\omega)$ has a peak when $\omega \rightarrow \omega_0$ ($\Delta \rightarrow 0$), where $|i\rangle$ is the state of maximum probability ($P_i \rightarrow 1$) at the π-pulse time.

Examining a plot for $P_i(\omega)$, we can carry out a search for the peak value of the probability (with an associated ω'-value). Then, for a particular value for the Rabi frequency Ω, ω' is the resonant frequency for the system. In other words $\omega' = \omega_0$. Conducting trials for different Rabi frequencies (we remind the reader that we accomplish this feat by varying the power input to an amplifier), we can observe the behavior of the state probabilities and the resonance in the weak and strong driving field regimes (Figure 4.7).

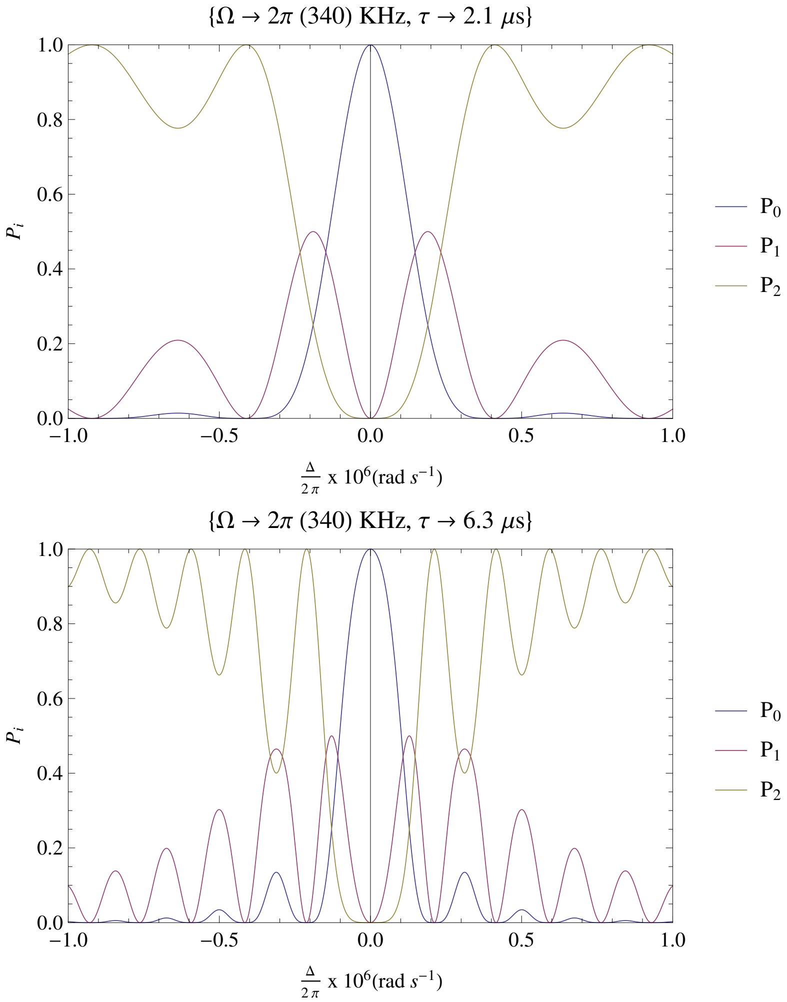

FIGURE 4.6. The comparison illustrates the importance of equation 4.15. The overall profile of the curves is similar, except the bottom plot has a narrower peak (corresponding to a bigger τ).

4.3. Concluding Remarks

This thesis is built around the notion of the Rabi frequency Ω. As we mentioned earlier, during an experiment, we do not directly control the Rabi frequency. We are in control of the input power to an amplifier which produces the electromagnetic (radio-frequency) field which couples the system. Therefore, it is vital to know the "Rabi Output" of our amplifier. In Figure 4.7, we plot the Rabi oscillations and find the Rabi frequency along with the input Power. The Rabi frequency values have been calculated by fitting analytical models to the Rabi oscillation experimental data for our ^{87}Rb isotope.

In Figure 4.7, we observe that the resonance of the system shifts with varying driving field strengths, plotted in 4.8. We present to the reader the calculated shifts, to indicate the scale of this resonance drift (Figures 4.9 and 4.10). Unexpectedly so, as the Rabi frequency Ω increases, the resonant frequency decreases. Our initial suspect, *the Bloch-Siegert shift*, affects the resonance on the order of a few kHz, and increases the resonant frequency as the Rabi frequency is increased. The cause of the Bloch-Siegert shift is not physical, but mathematical. When we invoke the rotating wave approximation, we drop the terms oscillating at twice the Rabi frequency. At high Rabi frequencies (strong driving fields), those doubly-oscillating terms (from the counter-rotating frame) start to matter and cause the Bloch-Siegert shift. The most likely cause for a fall in the resonance frequency with increasing Rabi frequency could be the presence of higher-order harmonics in the amplifier output. Given that the amplifier output data has not been compiled for such high input powers ($Power \rightarrow 3dBm$), it is impossible to tell if the amplifier output is clean.

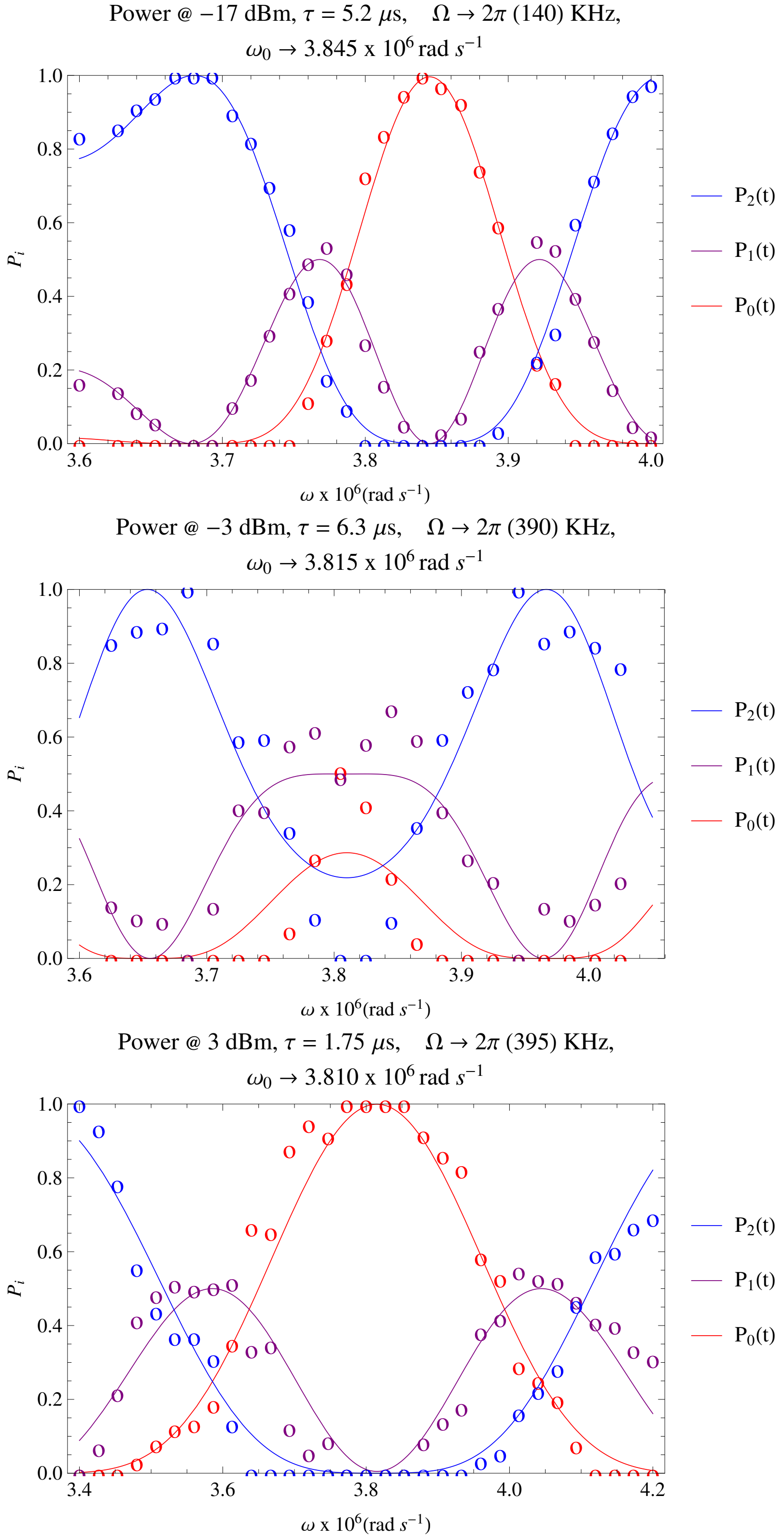

Power @ −17 dBm, $\tau = 5.2\ \mu s$, $\Omega \to 2\pi\ (140)$ KHz, $\omega_0 \to 3.845 \times 10^6\ \mathrm{rad}\ s^{-1}$

Power @ −3 dBm, $\tau = 6.3\ \mu s$, $\Omega \to 2\pi\ (390)$ KHz, $\omega_0 \to 3.815 \times 10^6\ \mathrm{rad}\ s^{-1}$

Power @ 3 dBm, $\tau = 1.75\ \mu s$, $\Omega \to 2\pi\ (395)$ KHz, $\omega_0 \to 3.810 \times 10^6\ \mathrm{rad}\ s^{-1}$

FIGURE 4.7. The data points represent the observed spectra in the Zeeman sublevels of the ^{87}Rb atom ground state for a fixed τ. The corresponding Rabi frequency, Ω and the resonant angular frequency ω_0 are found by fitting models; they are presented for each trial.

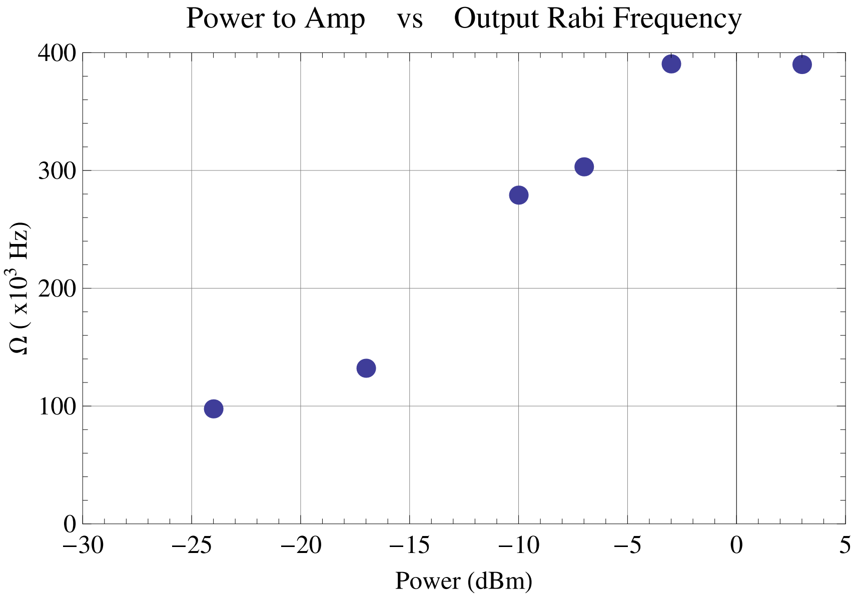

FIGURE 4.8. A representation of the Rabi output (Ω) of our amplifier, with respect to the input power of the amplifier (in dBm).

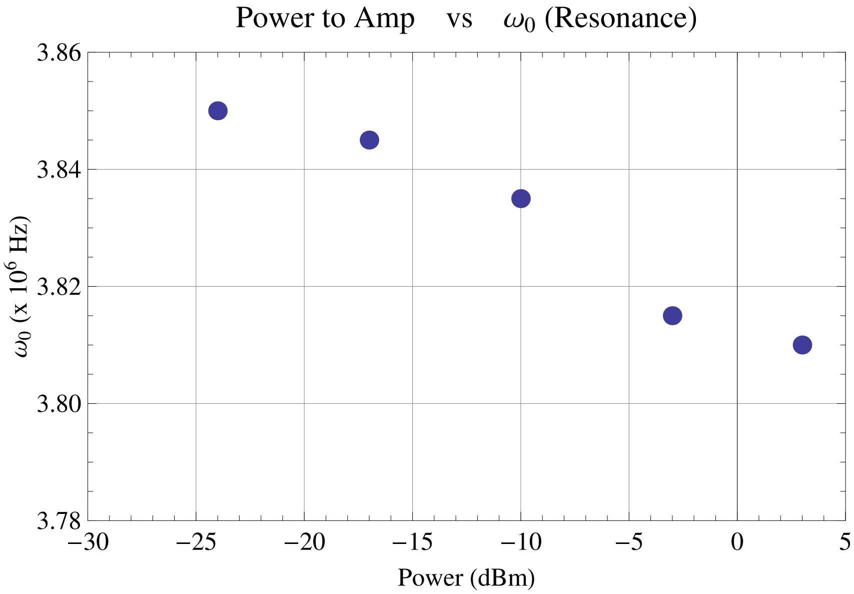

FIGURE 4.9. This plot shows the unexpected drift in the resonance (ω_0) as the amplifier input power (in dBm) is increased.

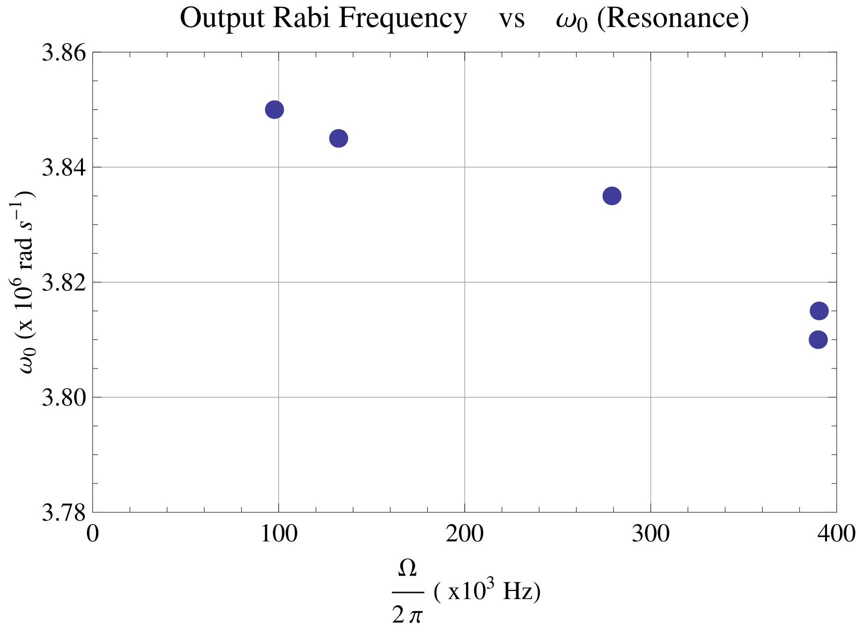

FIGURE 4.10. This plot shows the unexpected fall in the resonance frequency (ω_0), as the Rabi output frequency is increased.

Appendix: The Rotating Frame

The rotating frame, or the interaction picture is nothing more than a mathematical convenience and it does not affect the system in any way. As an analogy, it can be thought of as a frame in the Bloch sphere in which the Bloch vectors remain stationary, hence the name 'rotating frame'. We start by defining the unitary operator $\hat{U}$, for which $\hat{U}\hat{U}^* = \mathbb{I}$ and $\hat{U} = \hat{U}^*$.

$$\hat{U} = e^{\left[-\frac{i\hat{A}t}{\hbar}\right]}$$

In order for $\hat{U}$ to be a unitary, the operator $\hat{A}$ must be Hermitian with the property $\hat{A} = \hat{A}^*$. Now, starting with the system defined with $|\psi\rangle$, we redefine the system by operating on it with $\hat{U}$.

$$\left|\tilde{\psi}\right\rangle = \hat{U}^* \left|\psi\right\rangle$$

Note that since $\hat{U}$ is unitary, the wavefunction remains normalized and the probabilities (the observed results) are not affected by this transformation of the wavefunction:

$$\left|\left\langle \tilde{\psi} \,\middle|\, \tilde{\psi} \right\rangle\right|^2 = \left|\left\langle \psi^* \,\middle|\, \hat{U}\hat{U}^* \,\middle|\, \psi \right\rangle\right|^2 = \left|\left\langle \psi^* \,\middle|\, \psi \right\rangle\right|^2 = 1$$

In our derivation of the rotating frame Hamiltonian we will employ the Schrödinger equation for both $|\psi\rangle$ and $\left|\tilde{\psi}\right\rangle$:

$$\begin{aligned} i\hbar\frac{d}{dt}\left|\psi\right\rangle &= \hat{H}_0\left|\psi\right\rangle \\ i\hbar\frac{d}{dt}\left|\tilde{\psi}\right\rangle &= \hat{H}'\left|\tilde{\psi}\right\rangle \end{aligned}$$

Now we start with the Schrödinger equation and obtain a simplified expression for the rate of change of $\left|\tilde{\psi}\right\rangle$ on the right hand side of the equation below:

$$\begin{aligned} \hat{H}'\left|\tilde{\psi}\right\rangle &= i\hbar\frac{d}{dt}\left|\tilde{\psi}\right\rangle \\ &= i\hbar\frac{d}{dt}\left(\hat{U}^*\left|\psi\right\rangle\right) \\ &= i\hbar\left|\psi\right\rangle\frac{d}{dt}\hat{U}^* + i\hbar\hat{U}^*\frac{d}{dt}\left|\psi\right\rangle \\ &= \frac{i^2\hbar\hat{A}}{\hbar}\hat{U}^*\left|\psi\right\rangle + \hat{U}^* i\hbar\frac{d}{dt}\left|\psi\right\rangle \end{aligned}$$

Utilizing the Schrödinger equation for the original wavefunction $|\psi\rangle$, we substitute $\hat{H}|\psi\rangle$ for the Schrödinger factor in the last term:

$$\begin{aligned}
\hat{H}'\left|\tilde{\psi}\right\rangle &= -\hat{A}\hat{U}^{*}|\psi\rangle + \hat{U}^{*}\hat{H}_0|\psi\rangle \\
&= \hat{U}^{*}\hat{H}_0\mathbb{I}|\psi\rangle - \mathbb{I}\hat{A}\hat{U}^{*}|\psi\rangle \\
&= \hat{U}^{*}\hat{H}_0\hat{U}\hat{U}^{*}|\psi\rangle - \hat{A}\hat{U}^{*}|\psi\rangle \\
&= \left[\hat{U}^{*}\hat{H}_0\hat{U} - \hat{A}\right]\hat{U}^{*}|\psi\rangle \\
\hat{H}'\left|\tilde{\psi}\right\rangle &= \left[\hat{U}^{*}\hat{H}_0\hat{U} - \hat{A}\right]\left|\tilde{\psi}\right\rangle
\end{aligned}$$

It follows that:

$$\hat{H}' = \left[\hat{U}^{*}\hat{H}_0\hat{U} - \hat{A}\right]$$

For the last step, we once again invoke the properties of the hermitian operator $\hat{A}$ and the unitary operator $\hat{U}$. More specifically, we employ the relations $\hat{U} = \hat{U}^{*}$ and $\hat{A} = \hat{A}^{*}$.

$$\begin{aligned}
\hat{A} &= \left(\hat{A}\hat{U}^{*}\right)\hat{U} \\
&= \hat{U}\hat{A}^{*}\hat{U} \\
&= \hat{U}^{*}\hat{A}\hat{U}
\end{aligned}$$

Therefore, in the rotating frame or the interaction picture, the Hamiltonian $\hat{H}'$ is effectively the operator:

$$\hat{H}' = \left[\hat{U}^* \hat{H}_0 \hat{U} - \hat{U}^* \hat{A} \hat{U}\right]$$

$$\hat{H}' = \hat{U}^* \left[\hat{H}_0 - \hat{A}\right] \hat{U}$$

Bibliography

---

[1] Wolfgang Ketterle. Nobel lecture: When atoms behave as waves: Bose-einstein condensation and the atom laser. *Reviews of Modern Physics*, 74(4):1131–1151, 2002.

[2] Daniel A Steck. Rubidium 87 d line data, 2001.

[3] Jérôme Estève. Cold atoms: Trapped by nanostructures. *Nature nanotechnology*, 8(5):317–318, 2013.

[4] Augusto Smerzi, Stefano Fantoni, Stefano Giovanazzi, and SR Shenoy. Quantum coherent atomic tunneling between two trapped bose-einstein condensates. *Physical Review Letters*, 79(25):4950, 1997.

[5] Sathyandra Nath Bose. Planck's law and quantum light hypothesis. *Z. Phys*, 26:178–181, 1924.

[6] Albert Einstein. Bose-einstein statistics, prediction of bose-einstein condensate. *Sitzungsber. Kgl. Preuss. Akad. Wiss.*, 3, 1925.

[7] Louis De Broglie. Waves and quanta. *Comptes Rendes*, 177:507–510, 1923.

[8] D.R. TIlley and J. Tilley. *Superfluidity and Superconductivity.* Institute of Physics Publishing, NY, 1990.

[9] Evandro Agazzi. *Realism and Quantum Physics.* Rodopi B.V.Editions, 1997.

[10] Daniel V. Schroeder. *An Introductiion to Thermal Physics.* Addison-Wesley Publications, 1999.

[11] Charles Kittel and Herbert Kroemer. *Thermal Physics.* W. H. Freeman, 1980.

[12] Wolfgang Pauli. Nobel lecture. *Nobel Lectures, Physics*, pages 1942–1962, 1946.

[13] Clement J. Moses Raymond A. Serway and Curt A. Moyer. *Modern Physics.* Cengage Learning, 2004.

[14] A Cornell and Carl E Wieman. Nobel lecture: Bose-einstein condensation in a dilute gas, the first 70 years and some recent experiments. *Reviews of Modern Physics*, 74(3):875, 2002.

[15] K Kossert. Half-life measurements of 87-rubidium by liquid scintillation counting. *Applied radiation and isotopes*, 59(5):377–382, 2003.

[16] M.G. Mayer, SA Moszkowski, and LW Nordheim. Nuclear shell structure and beta-decay. i. odd a nuclei. *Reviews of Modern Physics*, 23(4):315, 1951.

[17] S Bize, Y Sortais, MS Santos, C Mandache, A Clairon, and C Salomon. High-accuracy measurement of the 87rb ground-state hyperfine splitting in an atomic fountain. *EPL (Europhysics Letters)*, 45(5):558, 1999.

[18] Mike H Anderson, Jason R Ensher, Michael R Matthews, Carl E Wieman, and Eric A Cornell. Observation of bose-einstein condensation in a dilute atomic vapor. *science*, 269(5221):198–201, 1995.

[19] Harold J Metcalf and Peter Van der Straten. *Laser cooling and trapping*. Springer, 1999.

[20] C. J. Foot. *Atomic Physics*. Oxford University Press, 2005.

[21] James R Anglin and Wolfgang Ketterle. Bose–einstein condensation of atomic gases. *Nature*, 416(6877):211–218, 2002.

[22] C.J. Pethick and A. Smith. *Bose-Einstein Condensation in Dilute Gases*. Cambridge University Press, 2002.

[23] J. Roger-Salazar. The gross-pitaeskii equation and bose-einstein condensates, 2013. Cornell arXiv:1301.2073.

[24] C Huepe, Stéphane Metens, Guy Dewel, Pierre Borckmans, and ME Brachet. Decay rates in attractive bose-einstein condensates. *Physical review letters*, 82(8):1616, 1999.

[25] H. Ragalla and Peter H Kes. *100 Years of Superconductivity*. CRC Press, 2012.

[26] Michael Tinkham. *Introduction to Superconductivity*. McGraw-Hill, 1975.

[27] David Shoenberg. *Superconductivity*. The University Press, 1952.

[28] Brian David Josephson. Possible new effects in supercoductive tunneling. *Physical Letters*, 1:251–253, 1962.

[29] Donald G. McDonald. The nobel laureate versus the graduate student. *Physics Today*, 54:47, 2001.

[30] Richard P. Feynman. *The Feynman Lectures on Physics*. Addison-Wesley Longman, 1970.

[31] David J. Griffiths. *Introduction to Quantum Mechanics*. Pearson Prentice Hall (2nd Edition), 2004.